

# Seismic anisotropy of the crust: electron-backscatter diffraction measurements from the Basin and Range

Monica E. Erdman,<sup>1,\*</sup> Bradley R. Hacker,<sup>1</sup> George Zandt<sup>2</sup> and Gareth Seward<sup>1</sup>

<sup>1</sup>Earth Science, University of California, Santa Barbara, CA 93106, USA. E-mail: mee5@rice.edu

<sup>2</sup>Geosciences, University of Arizona, Tucson, AZ 85721, USA

Accepted 2013 July 15. Received 2013 July 12; in original form 2013 April 23

## SUMMARY

Crystal preferred orientations were measured in a suite of rocks from three locations in the Basin and Range using electron-backscatter diffraction. Anisotropic velocities were calculated for all rocks using single-crystal stiffnesses, the Christoffel equation and Voigt–Reuss–Hill averaging. Anisotropic velocities were calculated for all three crustal sections using these values combined with rock proportions as exposed in the field. One suite of rocks previously measured in the laboratory was used as a benchmark to evaluate the accuracy of the calculated velocities.

Differences in the seismic anisotropy of the Funeral Mountains, Ruby Mountains and East Humboldt Range sections arise because of differences in mineralogy and strain, with the calcisilicate dominated Ruby Mountains section having higher  $P$ -wave speeds and  $V_p/V_s$  ratios because of the reduced quartz content. In all cases, the velocities show either transverse isotropy or nearly so, with a unique slow axis normal to the foliation. Velocity anisotropy can thus be used to infer the flow plane, but not the flow direction in typical crustal rocks. Areas with a subhorizontal foliation have minimal shear wave splitting for vertically propagating waves and are thus good places to measure mantle anisotropy using SKS-splitting.

**Key words:** Composition of the continental crust; Creep and deformation; Seismic anisotropy; North America.

## INTRODUCTION

The symmetry, magnitude and spatial variation of seismic anisotropy in Earth provide the means to investigate thermal, compositional and kinematic variations arising from plate tectonics and crust–mantle interactions (e.g. Schulte-Pelkum *et al.* 2005; Xu *et al.* 2007; Karato *et al.* 2008). For example, shear wave splitting of teleseismic waves propagated through the mantle are often interpreted in terms of mantle flow (e.g. Long & Silver 2008, 2009). The logic is that mantle flow produces a preferred alignment of elastically anisotropic olivine crystals, which produces anisotropic wave propagation (e.g. Christensen 1984; Nicolas & Christensen 1987; Zhang & Karato 1995; Silver 1996; Savage 1999; Karato *et al.* 2008). The predominant slip systems in olivine produce orthorhombic velocity anisotropy, with the fast propagation direction parallel to the olivine flow direction (e.g. Mehl *et al.* 2003). The fast polarization plane of split shear waves is thus often used to infer flow within the mantle.

Though first observed in the 1960s (e.g. Hasbrouck 1964), technological advancements now enable more routine measurements of mid to lower crustal anisotropy. Seismic studies in western North

America have detected crustal seismic anisotropy using Pn tomography (Hearn 1996), teleseismic receiver functions (McNamara & Owens 1993; Porter *et al.* 2011), local earthquake  $S$ -wave splitting (Currie *et al.* 2004) and ambient noise tomography (Moschetti 2010).

Numerous workers have employed the pulse-transmission (PT) technique to rocks in order to relate petrophysical observations to anisotropy in the crust (e.g. Christensen 1965; Burlini & Fountain 1993; Ji *et al.* 1993; Barruol & Kern 1996; Burlini *et al.* 1998; Ivankina *et al.* 2005). This approach is excellent in many ways, but compromised by sample variability, alteration, cracks and (usually) a limitation to three orthogonal directions. An alternative approach to determining the elastic properties of rocks is to measure the crystal preferred orientations (CPOs) of the constituent phases and then calculate rock elasticity from single-crystal stiffnesses (Mainprice & Nicolas 1989). Recent advances in electron-backscatter diffraction (EBSD) enable the complete and rapid characterization of the orientations, composition and abundances of all minerals in a polycrystalline aggregate. From these parameters, the stiffness tensor of the bulk rock may be calculated, allowing the 3-D seismic properties of the rock to be determined as well. Because this method uses single-crystal elastic constants to determine bulk properties, it allows for the relationship between microstructure, fabric and

\*Now at: Earth Science, Rice University, Houston, TX 77005, USA.

seismic properties to be analysed. This paper calculates the velocity anisotropy of three Basin and Range lower crustal sections, and—in conjunction with other work—shows how the magnitude and symmetry of lower crustal velocity anisotropy can be interpreted in terms of rock composition, temperature and/or material flow.

## GEOLOGICAL SETTING

The metamorphic core complex belt of the Basin and Range Province in the western United States exposes metamorphic rocks (Coney & Harms 1984) buried during Late Jurassic–Cretaceous shortening and exhumed during the Tertiary (Wright & Snoke 1993; Applegate & Hodges 1995). We collected samples from the Funeral Mountains of Death Valley, California and the Ruby–East Humboldt Range (Ruby–EHR) of northeastern Nevada. Both areas experienced metamorphic conditions typical of the lower crust: the Funeral Mountains reached peak metamorphic conditions of  $650\text{ }^{\circ}\text{C}$  and  $7\text{--}9\text{ kbar}$  or  $\sim 25\text{--}33\text{ km}$  depth (Hodges & Walker 1990; Mattinson *et al.* 2007) and the Ruby–EHR reached peak metamorphic conditions of  $>9\text{ kbar}$  ( $\sim 33\text{ km}$  depth) and  $800\text{ }^{\circ}\text{C}$  (McGrew *et al.* 2000). The Funeral Mountain samples were collected from the structurally deepest unit in Monarch Canyon, in which mixed orthogneiss and paragneiss are intruded by leucogranite (Fig. 1). The foliation dips about  $35^{\circ}$  to the northeast and the lineation plunges down dip; the entire section sampled is  $\sim 500\text{ m}$  thick. The Ruby–EHR samples were collected from Angel Lake cirque, Lizzie’s Basin and Lamoille Canyon, where orthogneiss, dolomitic marble, paragneiss, metaquartzite and calc-silicate rocks are intruded by leucogranite (Snoke *et al.* 1997) (Fig. 2). In the Ruby Mountains, the average foliation dips  $\sim 5^{\circ}$  to the west, the lineation plunges  $5^{\circ}$  towards

$345^{\circ}$  and the sampled section is  $\sim 1000\text{ m}$  thick. The EHR section is  $1050\text{ m}$  thick, the foliation dips  $10^{\circ}$  to the northeast and the lineation trends  $125^{\circ}$ .

## ANALYTICAL METHODS

A suite of representative oriented samples was collected at each study site. The samples were cut into  $XZ$  (parallel to lineation and normal to foliation) or  $XY$  (parallel to foliation) thin sections depending on the abundance of mica;  $XY$  sections are preferable for samples with abundant mica because diffraction patterns from  $[001]$  zones in mica are easier to measure than  $(hk0)$  zones. The thin sections were polished with  $0.25\text{ }\mu\text{m}$  diamond, colloidal silica and coated with  $6\text{--}10\text{ nm}$  of carbon. The CPOs were measured at the University of California, Santa Barbara with an HKL Technology EBSD detector and Channel 5 software on an FEI Quanta 400f field-emission scanning electron microscope. All EBSD measurements were made with a  $70^{\circ}$  sample tilt, a  $15\text{-mm}$  working distance,  $100\times$  magnification, a  $1\text{--}3\text{ nA}$  beam current and a  $20\text{ kV}$  accelerating voltage. The step size ( $250\text{--}500\text{ }\mu\text{m}$ ) and the mapped area were scaled based on the grain size, with the objective of analysing a large area and a large number of grains in a reasonable length of time. Every diffraction pattern was saved. Before each automated run, tens of grains were measured manually to verify that the calculated diffraction patterns fit the observed Kikuchi bands.

All mineral compositions were measured by energy-dispersive spectrometry (EDS) simultaneously with the EBSD measurements. This is necessary to ensure that every point is correctly indexed. After the data collection was complete, the entire dataset was processed with a Matlab algorithm that used the EDS spectrum ( $500\text{-ms}$

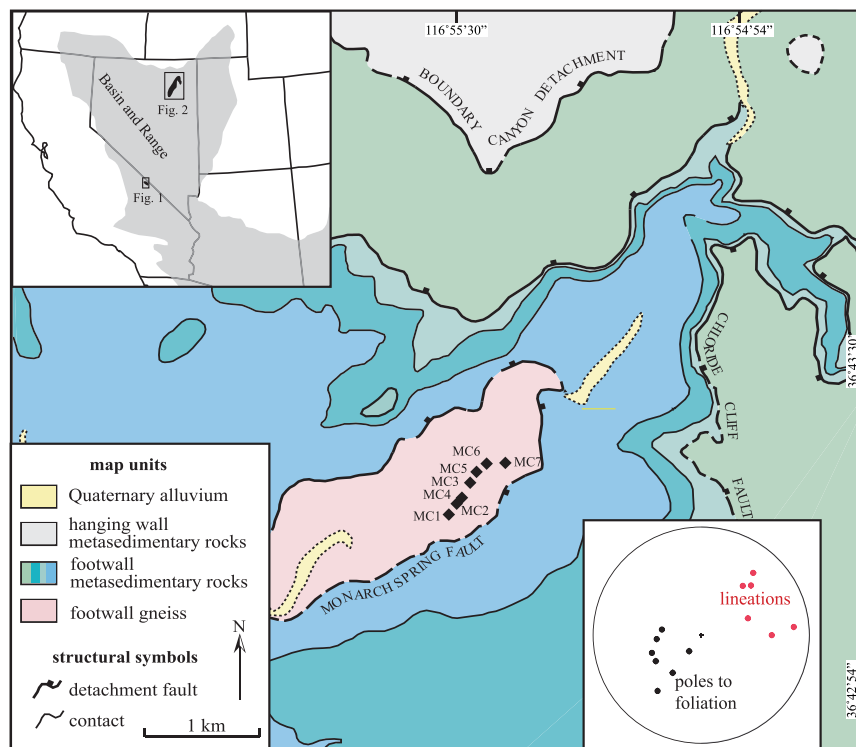


**Figure 1.** Geological map of Monarch Canyon in the Funeral Mountains, Death Valley, California (modified from Mattinson *et al.* 2007) with rock fabric data. Sample locations are all from the structurally lowest unit, which has a gently NE-dipping foliation and NE-plunging lineation. Inset shows study areas within the Basin and Range Province.

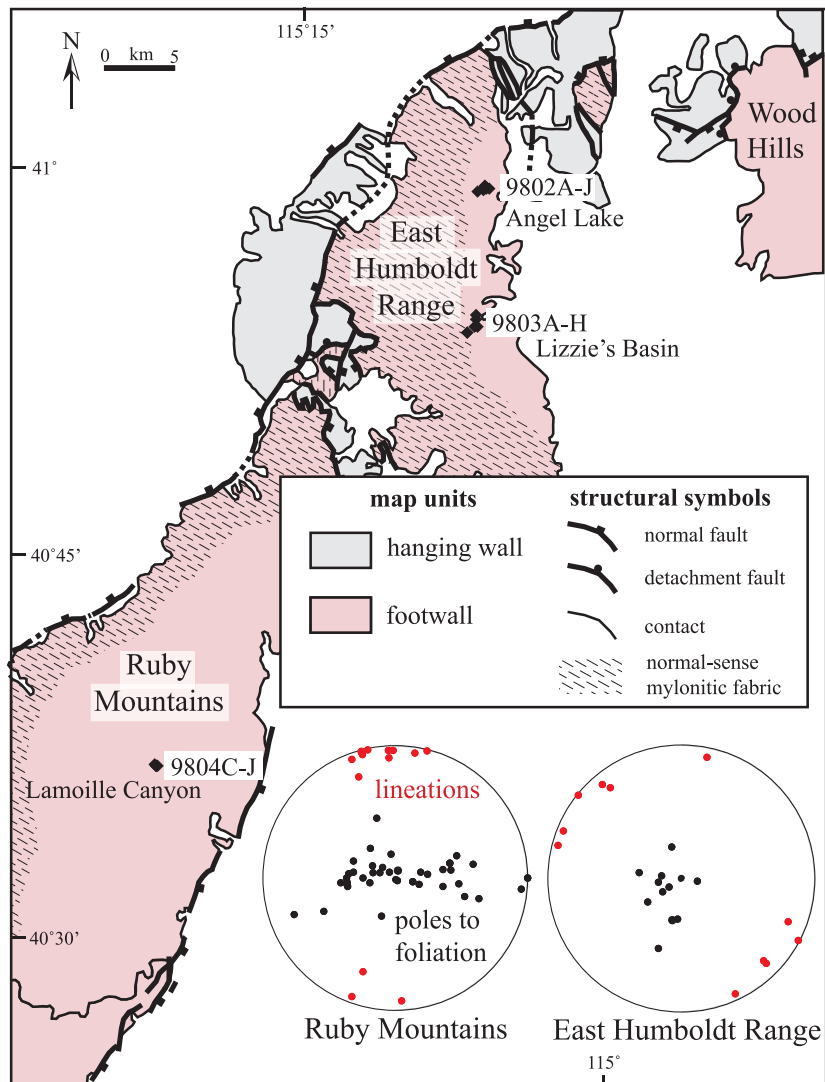


**Figure 2.** Geological map of the Ruby–East Humboldt Range in northeastern Nevada (modified from Sullivan & Snoko 2007). Sample locations are all from the structurally lowest unit, which has a flat-lying foliation and N- or NW-trending lineation.

exposure time) to identify the mineral at each point (Brownlee *et al.* 2011). The saved diffraction patterns were then reindexed with the EBSD software based on the cell parameters for that phase only. Phase proportions determined by this method agree well with results from point counting. Skipping this tedious method—and assuming that the HKL software correctly identifies minerals based only on diffraction patterns—leads to calculated rock velocities that are inaccurate by as much as  $0.4 \text{ km s}^{-1}$  and calculated anisotropies that are inaccurate by as much as a factor of 2 (this study).

The elasticity of each sample was calculated from the measured CPOs and the abundances of the constituent minerals (Table 1) by solving the Christoffel equation (Crosson & Lin 1971) using the software of Mainprice (1990). The results reported here are Voigt–Reuss–Hill averages computed from the single-crystal elastic constants and densities listed in Table 2. Elastic constants for labradorite ( $An_{57}$ ) were used for the Funeral Mountains samples (after plagioclase compositions reported in Mattinson *et al.* 2007), and the elastic constants for albite and anorthite were used for siliclastic and calc-silicate rocks, respectively, for the Ruby–EHR, following measurements by Hodges *et al.* (1992) and Hudec (1992).

The elastic properties of the individual rocks were then combined in their outcrop proportions and respective orientations to yield the average elastic properties of the Funeral Mountains, Ruby Mountains and EHR crustal sections. Table 1 summarizes the proportions used in the calculations as well as the calculated maximum and minimum  $P$ -wave velocities and  $P$ - and  $S$ -wave anisotropy. Elastic tensors for individual rocks and crustal sections are given in Table S1.

The Funeral Mountains study site is characterized by quartzofeldspathic orthogneiss with varying biotite content (represented by samples MC1, MC2, MC4, MC5 and MC7), 1 per cent garnet-bearing gneiss (MC3) and  $\sim 10$  per cent discordant leucosomes (MC6) that are up to 30 Myr younger than the peak metamorphism (Mattinson *et al.* 2007). The Ruby Mountains at the road end in Lamoille Canyon are composed of  $\sim 80$  per cent carbonate and calc-silicate gneiss (samples 9804C–9804G) and 20 per cent quartzofeldspathic gneiss (9804I). These rocks are intruded by equigranular and pegmatitic leucogranites (9804J) that make up a significant amount of the exposed section, ranging from 95 per cent at lower structural levels to 10 per cent at higher levels. The EHR is composed of a sequence of orthogneiss, paragneiss and



**Table 2.** Mineral abbreviations, densities and elastic stiffnesses.

Mineral	Abbreviation	Density (g cm <sup>-3</sup> )	Source for $C_{ij}$
Albite ( $An_{00}$ )	ab	2.62	Brown <i>et al.</i> (2007)
Anorthite ( $An_{100}$ )	an	2.76	Hearmon (1984)
Biotite	bi	3.05	Belikov <i>et al.</i> (1970)
Calcite	cc	2.71	Dandekar (1968)
Chlorite	chl	2.8	Aleksandrov & Ryzhova (1961); Theye <i>et al.</i> (2003)
Clinopyroxene	cpx	3.33	Collins & Brown (1998)
Dolomite	do	2.795	Humbert & Plique (1972)
Epidote (zoisite)	ep	3.34	Mao <i>et al.</i> (2007)
Garnet	gar	4.16	Babuska <i>et al.</i> (1978)
Hornblende/tremolite	hb/tre	3.12	Aleksandrov & Ryzhova (1961)
K-feldspar	kfs	2.62	Aleksandrov <i>et al.</i> (1974)
Labradorite ( $An_{57}$ )	lbr	2.7	Ryzhova (1964)
Muscovite	mu	2.84	Vaughan & Guggenheim (1986)
Quartz	qz	2.65	Lakshtanov <i>et al.</i> (2007)
Sillimanite	sill	3.24	Vaughan & Weidner (1978)
Sphene/rutile	sph	4.26	Bass (1995)

metaquartzite (typified by samples 9802A, 9802B, 9802G, 9802I and 9803A, 9803G and 9803H) with a thin,  $\sim 10$  m thick, carbonate section of calcitic and dolomitic marble (9802E, 9802C and 9803E). Discordant leucogranites and pegmatites (9802H, 9802J and 9803B, 9803C) comprise up to 50 per cent of some units. The Angel Lake and Lizzie's Basin study sites expose similar rocks; the proportions of rock types were determined from field observations using a map provided by Allen McGrew (private communication 2011).

## ACCURACY OF EBSD-BASED VELOCITY CALCULATIONS

How do the velocities calculated from EBSD-determined CPOs, single-crystal stiffnesses and Voigt–Reuss–Hill average compare to velocities measured directly from rocks in the laboratory? To assess this, some of the Ruby Mountains samples analysed by McDonough & Fountain (1993) via the PT technique were re-analysed in this study (Table 3). For each sample, we measured the CPOs and mineral proportions and then calculated velocities, as described above. Fig. 3 compares the measured (dashed) and calculated (solid)  $P$ -wave velocities for several samples. The dashed lines follow the characteristic non-linear increase in velocity at low confining pressure (attributed to crack closure; Birch 1960) followed by a more gradual linear increase at high pressure. Because our calculated velocities are derived from single-crystal elastic constants measured at atmospheric pressure, they must be extrapolated to the pressures of the PT measurements before a direct comparison is possible. We assume a linear velocity increase with pressure:  $V_{600} = V_0 + P(\partial V/\partial P)$ , where  $V_{600}$  is the extrapolated velocity at 600 MPa,  $V_0$  is the velocity at 1 atm and  $\partial V/\partial P$  is calculated for each sample using the algorithm of Hacker & Abers (2004). The solid lines in Fig. 3 show the results of this extrapolation in the same three orthogonal directions measured by McDonough & Fountain (1993).

The measured and calculated values agree to within 2.5 per cent (or  $0.15 \text{ km s}^{-1}$ ) on average, with a maximum difference of 8 per cent ( $0.48 \text{ km s}^{-1}$ ). The calculated velocities are consistently slower than the measured velocities; this may be due to the relative paucity of plagioclase elasticity measurements, uncertainties in modal abundance, or uncertainties in  $\partial V/\partial P$ . If one desired, the velocities reported below could be corrected upward by  $+0.15 \text{ km s}^{-1}$ .

Godfrey *et al.* (2000) concluded that measuring velocities in only three principal directions (parallel to the sample  $X$ ,  $Y$  and  $Z$  directions) does not describe the complete elastic anisotropy of a rock; such measurements are blind to elastic properties not aligned with those directions. Comparison of Fig. 3 with the figures that follow shows that, in this study, measuring velocities in three orthogonal directions *only* can underestimate elastic anisotropy by as much as 5.5 percentage points—a factor of 30. Such discrepancies illustrate the importance of determining the full 3-D elastic anisotropy of rocks.

## MEASURED CPOs

### Funeral Mountains

The samples analysed from the Funeral Mountains comprise six quartzofeldspathic gneisses and a single leucogranite (Table 1). The gneisses are characterized by K-feldspar porphyroclasts in a matrix of equant, smaller quartz and plagioclase and distributed, aligned mica. The CPOs of these rocks are shown as either inverse pole figures or pole figures (Fig. 4; Figs S1–S4). Most of the CPOs are nearly symmetric with respect to the foliation and lineation, implying near-coaxial deformation (Lister & Hobbs 1980; Passchier & Trouw 1996). Biotite and muscovite have (001) maxima perpendicular to the foliation and either [100] maxima, [110] maxima, or an [hk0] girdle subparallel to the lineation, suggesting chiefly [hk0](001) slip. Sillimanite has a (010) maximum parallel to the foliation and a [001] maximum parallel to the lineation, compatible with [001](010) slip. The quartz CPOs for two samples (MC3 and MC7) are dominated by a [c] axis maximum parallel to  $Y$ , and (a) maxima symmetrically disposed about  $X$ , suggesting dominantly prism (a) slip. The quartz CPO for sample MC6 has a crossed girdle of [c] axes and two (a) axis maxima symmetrically disposed about the lineation, implying mixed (a) slip during coaxial plane strain (Barth *et al.* 2010). The quartz CPOs for the other Monarch Canyon samples are weaker (multiples of uniform distribution, MUD, less than 3) and less clearly defined. Thermobarometric studies suggest that this Funeral Mountains suite reached peak metamorphic temperatures of  $630^\circ\text{C}$  (Mattinson *et al.* 2007), but the quartz CPOs are not typical of those formed by deformation at such high temperature (Lister *et al.* 1978; Schmid & Casey 1986); the CPOs may therefore reflect deformation during cooling.

**Table 3.** Calculated velocities for Ruby-EHR samples determined in this study; compare to Table 2 of McDonough & Fountain (1993).

Sample	Mineralogy (per cent) and rock type	$AV_P$ (per cent)	$AV_{S_{max}}$ (per cent)		$V_P$ (km s <sup>-1</sup> ) at 0 MPa	$V_P$ (km s <sup>-1</sup> ) at 600 MPa
RM-1	44 qz, 34 pl, 15 kfs, 7 mu gneiss	3.0	4.81	X	6.04	6.12
				Y	6.18	6.26
				Z	6.05	6.13
RM-6	48 pl, 25 qz, 16 kfs, 11 bi gneiss	4.4	5.58	X	6.01	6.12
				Y	6.05	6.16
				Z	6.14	6.25
RM-7	85 qz, 10 kfs, 3 pl, 1 mu, 1 bi quartzite	9.7	13.07	X	5.82	5.87
				Y	6.20	6.25
				Z	6.02	6.07
RM-10	35.4 pl, 30 qz, 24 kfs, 10 mu, 0.6 gar gneiss	5.6	4.34	X	6.15	6.23
				Y	6.14	6.22
				Z	6.15	6.23
RM-16	46 pl, 29 qz, 19 kfs, 6 bi quartz monzonite	5.1	6.26	X	5.96	6.05
				Y	6.04	6.13
				Z	6.16	6.25
RM-19	86 qz, 10 kfs, 3 bi, 1 pl quartzite	10.5	12.84	X	5.95	5.99
				Y	6.25	6.29
				Z	5.88	5.92
RM-26	60 pl, 21 hb, 14 bi, 2 qz, 1.5 ep, 1.3 sph schist	6.5	10.50	X	6.45	6.57
				Y	6.19	6.31
				Z	6.35	6.47
RM-28	36 qz, 32 pl, 22 kfs, 10 bi gneiss	6.2	10.08	X	6.04	6.13
				Y	6.13	6.22
				Z	5.93	6.02
RM-29	79 qz, 11 bi, 10 pl micaceous quartzite	12.6	19.04	X	6.00	6.06
				Y	6.24	6.30
				Z	5.81	5.87
RM-36	49 pl, 19 bi, 18 qz, 9 kfs, 4 hb biotite gneiss	9.4	14.53	X	6.16	6.27
				Y	6.27	6.38
				Z	6.02	6.13
RM-37	68 pl, 18 bi, 8 kfs, 3 qz, 2 hb, 0.2 zr, 0.2 sph tonalite	6.7	8.49	X	5.95	6.42
				Y	6.29	6.26
				Z	6.13	6.14

The plagioclase and K-feldspar CPOs are less straightforward to interpret. Perhaps the most consistent feature is a (010) maximum parallel to the foliation (MC1, MC6, MC7 plagioclase and MC2 K-feldspar); a few samples also have (001) maxima near the lineation. The CPOs are compatible with a range of slip systems, dominated by slip along (010). K-feldspar CPOs are asymmetric with respect to the rock fabric, deviating by as much as 30° (e.g. MC2, MC7).

### Ruby Mountains

Seven samples from Lamoille Canyon were analysed to characterize the Ruby Mountains (Fig. 2). These samples are dominantly calc-silicates, but three quartzofeldspathic gneiss and a leucogranite were also analysed (Table 1). The calc-silicates are characterized by diopside porphyroclasts in a matrix of equant, smaller quartz and carbonate minerals, and distributed, aligned mica. Most of the CPOs (Fig. 5; Figs S5–S7) are asymmetric with respect to the foliation by up to 20°, implying non-coaxial deformation (Lister & Hobbs 1980; Passchier & Trouw 1996). Biotite displays a (001) maximum perpendicular to the foliation and a broad [100] maximum around the lineation, consistent with [100](001) slip. In three samples, clinopyroxene has a [001] maximum parallel to the lineation

and (100), (110) or ( $\bar{1}11$ ) maxima parallel to the foliation, implying [001](hk0) pencil glide. Clinopyroxene in a fourth sample (9804E) shows a broad [010] to [011] maximum perpendicular to the foliation and a [100] maximum parallel to the lineation, compatible with [100](0kl) slip. The hornblende CPO from 9804E has [100] subparallel to the lineation, and an (0kl) girdle perpendicular to the foliation, compatible with [100](0kl) slip. Calcite in two samples has a moderate [c] axis maximum perpendicular to the foliation and a girdle of lineation directions subperpendicular to [c], suggesting slip on ⟨a⟩ directions along (0001). Plagioclase CPOs are somewhat diffuse, but the simplest have [100] or [010] maxima parallel to the lineation and a [001] maximum perpendicular to foliation, suggesting ⟨uv0⟩(001) slip.

Quartz CPOs vary considerably. In two samples (9804I and 9804E), quartz has a [c] axis maximum parallel to the lineation, suggesting dominantly prism [c] slip. A single sample (9804J) has a quartz CPO dominated by a [c] axis maximum parallel to Y, indicative of prism ⟨a⟩ slip. Sample 9804G shows a crossed girdle of [c] axes and two ⟨a⟩ axis maxima, suggesting mixed ⟨a⟩ slip. Thermobarometry suggests that these rocks reached peak metamorphic conditions of 800 °C (McGrew *et al.* 2000), and the quartz CPOs in 9804I and 9804E are compatible with deformation at such temperatures (Lister *et al.* 1978; Schmid & Casey 1986).

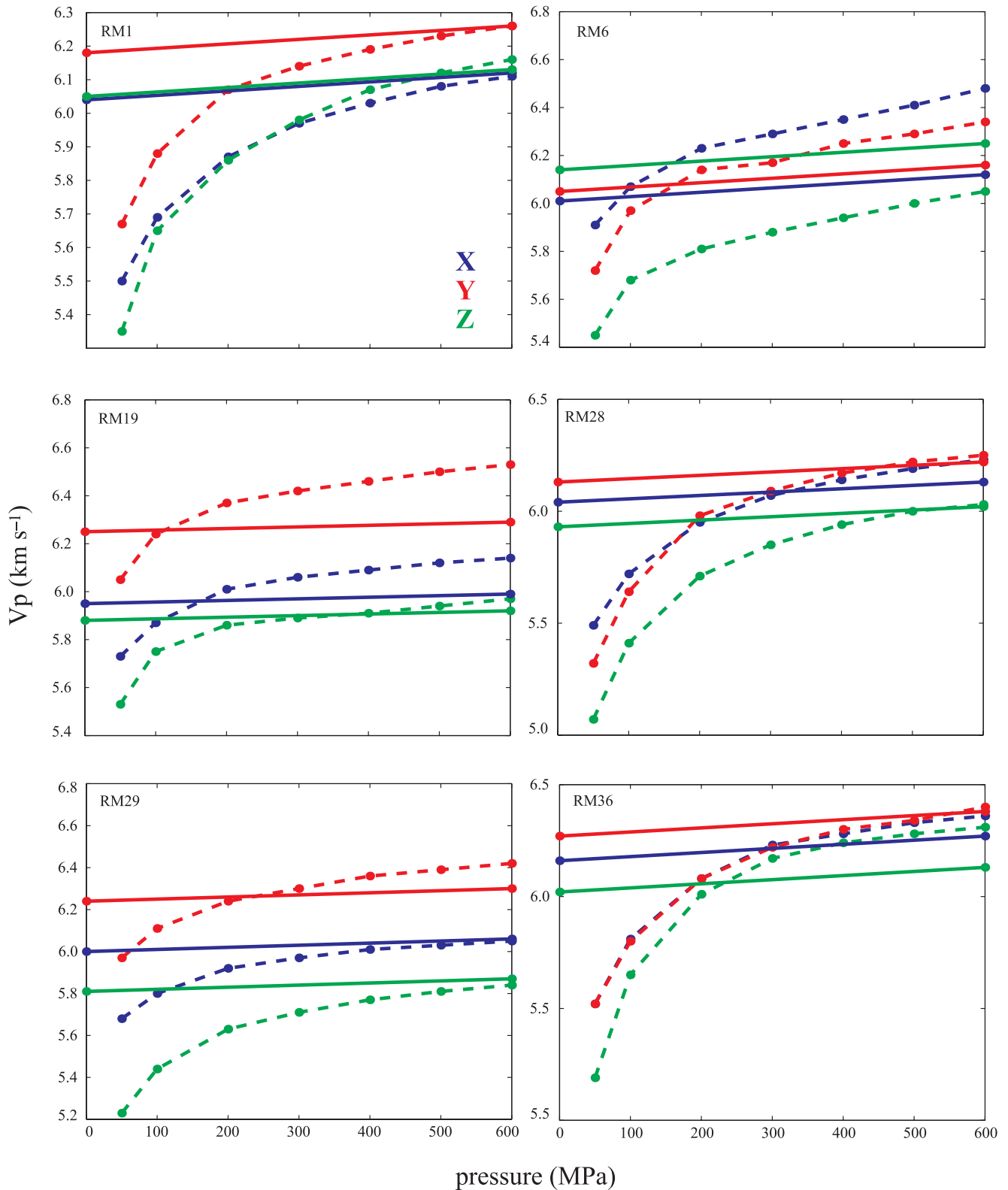


**Figure 3.** Representative measured compressional wave velocities (dashed lines; McDonough & Fountain 1993) and calculated velocities (solid lines; this study, Table 3).  $X$  is parallel to the lineation,  $Y$  is parallel to the foliation and normal to the lineation and  $Z$  is normal to the foliation. Calculated values at zero pressure from EBSD data are extrapolated to high pressure using  $\partial V_p/\partial P$  determined via Hacker & Abers (2004).

### EHR

Fifteen samples were collected to characterize the EHR. The samples are principally quartzofeldspathic gneiss, but include three

calc-silicates, two leucogranites and a granodiorite (Table 1). The gneisses are characterized by relatively equigranular quartz and feldspar and distributed, aligned mica. The CPOs of minerals in

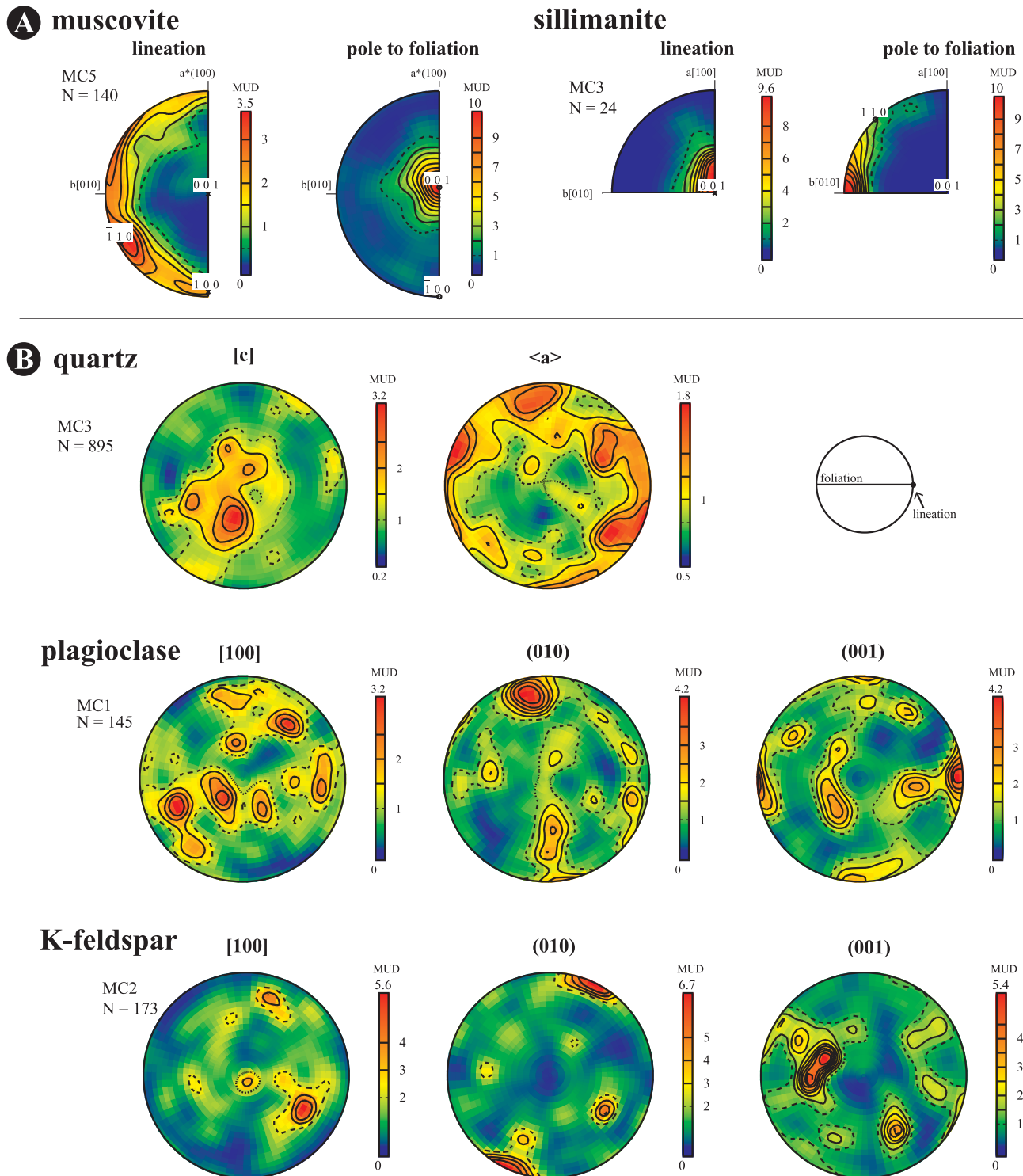


**Figure 4.** Representative CPOs of common minerals in the Funeral Mountains samples. (a) Muscovite and sillimanite inverse pole figures for lineations and poles to foliation planes. Crystallographic directions are marked; “\*” indicates a direction normal to a plane (e.g.  $a^*(100)$  indicates the normal to the (100) plane). (b) Equal-area, lower hemisphere pole figures for quartz, plagioclase and K-feldspar CPOs, with foliation and lineation orientated as shown. (010) and (001) refer to the pole to the (010) and (001) planes, respectively. Shading scale is in multiples of uniform distribution (MUD).

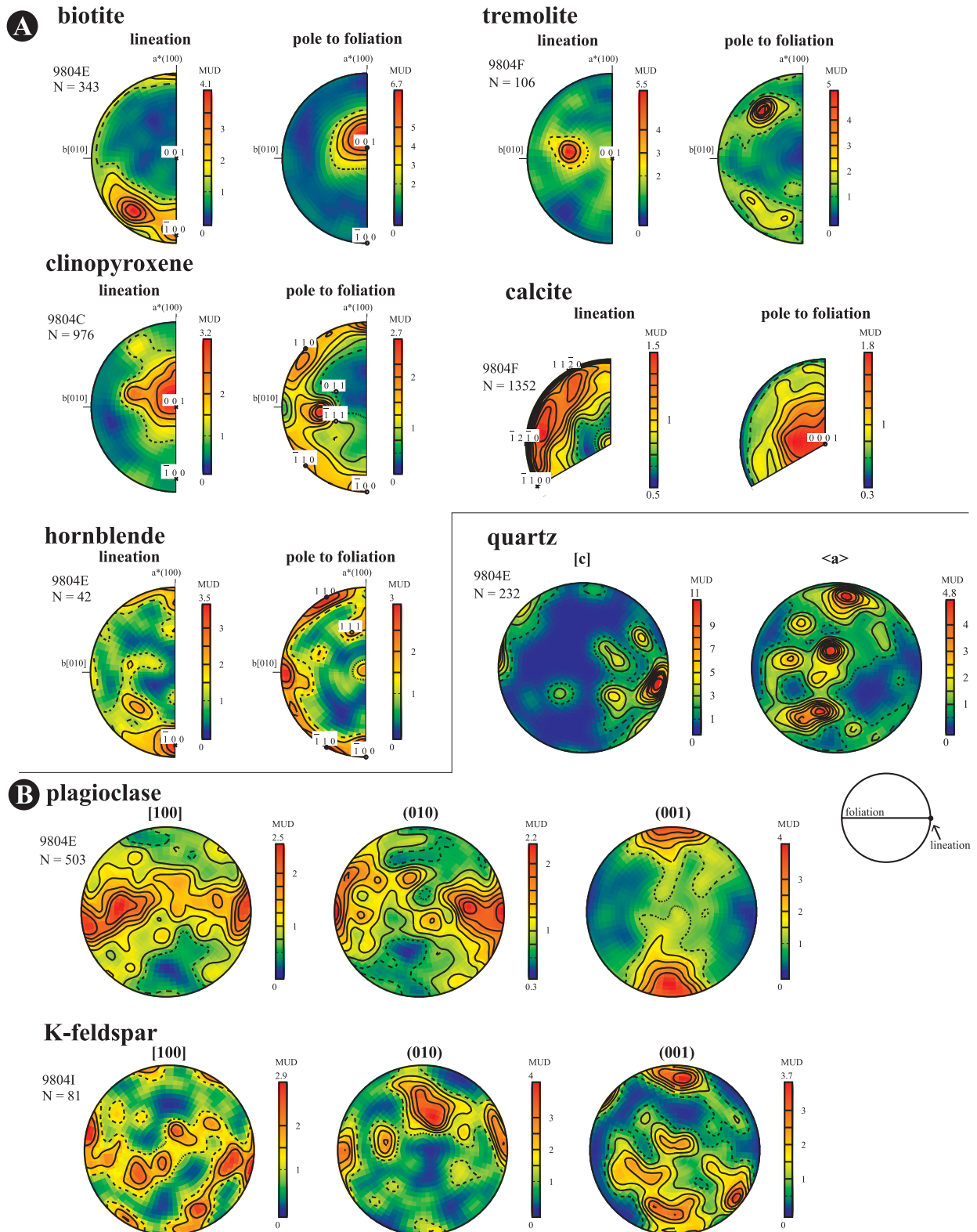


**Figure 5.** Representative CPOs of common minerals in the Ruby Mountains samples. (a) Biotite, tremolite, clinopyroxene, calcite and hornblende inverse pole figures for lineations and poles to the foliation. (b) Equal-area, lower hemisphere pole figures for quartz, plagioclase and K-feldspar.

this region (Fig. 6; Figs S8–S11) are asymmetric with respect to the foliation by up to 40°, implying non-coaxial deformation (Lister & Hobbs 1980; Passchier & Trouw 1996). Biotite and muscovite typically show either a single, broad [100] maximum parallel to the

lineation or a girdle of [uv0] directions subparallel to the lineation; (001) is invariably perpendicular to the foliation, implying slip along (001) in directions dominated by [100] and [010]. K-feldspar shows two kinds of CPO. Most commonly (9802H, 9802I, 9803C),

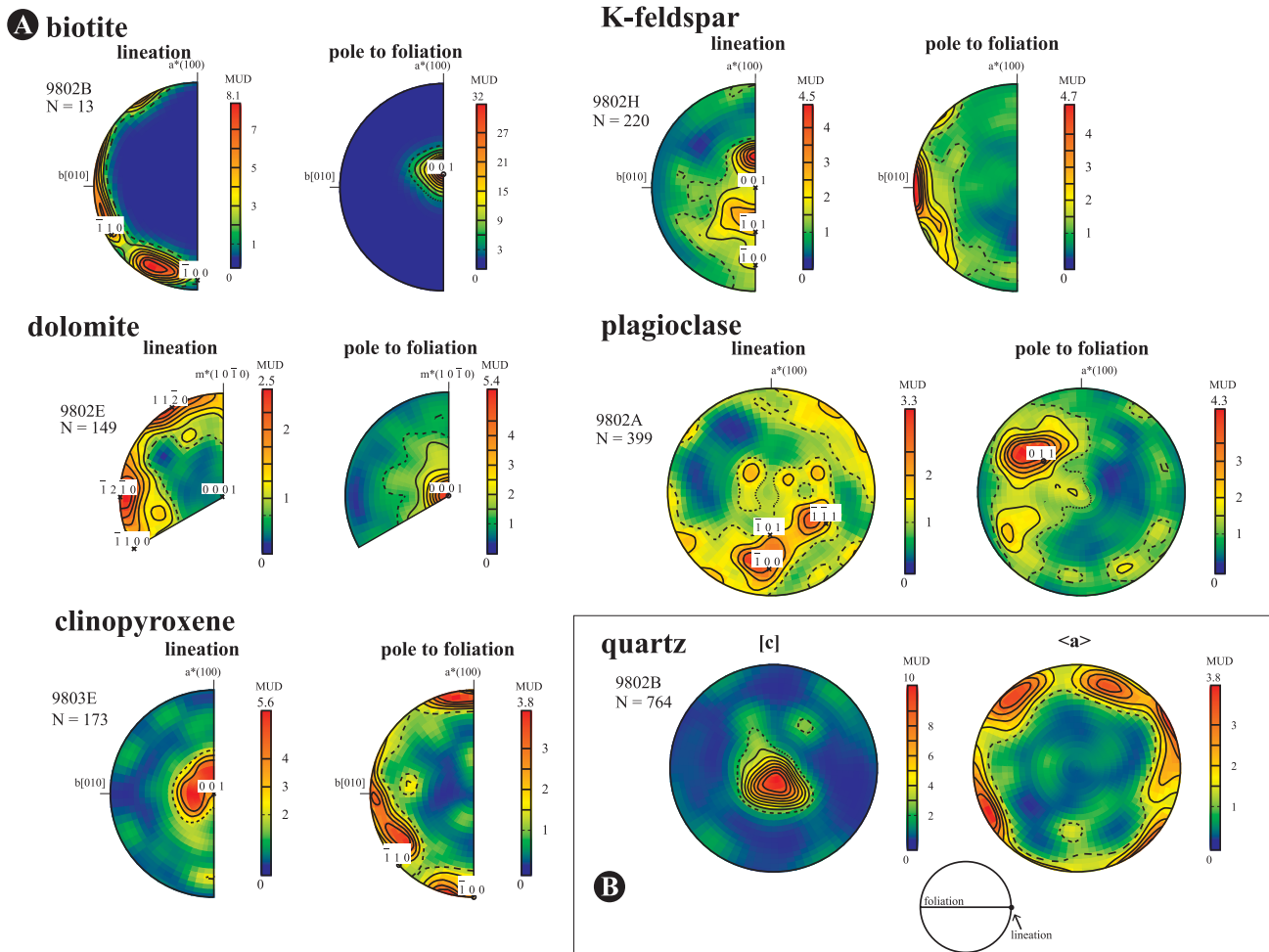


**Figure 6.** Representative CPOs of common minerals in the East Humboldt Range samples. (a) Inverse pole figures for lineations and poles to the foliation. (b) Equal-area, lower hemisphere pole figures for quartz.

K-feldspar displays either a (010) maximum, (110) and  $(\bar{1}\bar{1}0)$  maxima, or all three parallel to the foliation, with some combination of [001] and  $[\bar{1}01]$  maxima subparallel to the lineation; these CPOs suggest slip on a variety of systems dominated by [001](010).

The most common plagioclase CPO consists of (011) or nearby planes parallel to the foliation and  $[\bar{1}00]$  to  $[\bar{1}\bar{1}1]$  direction parallel to the lineation, compatible with  $[\bar{1}00]$  to  $[\bar{1}\bar{1}1](011)$  slip. Calcite and dolomite show a simple CPO in a single sample (9802E), with an  $\langle a \rangle$  maximum parallel to the lineation and a  $[c]$  maximum perpendicular to the foliation, indicative of  $\langle a \rangle$  (0001) slip; the two other calcite CPOs are more complex. Clinopyroxene has a [001] maximum parallel to the lineation and [010] and [100] maxima perpendicular to the foliation, suggesting slip in the [001] direction on the (010) and (100) planes.

In all but one sample, quartz shows a  $[c]$  axis maximum subparallel to  $Y$ , indicative of prism  $\langle a \rangle$  slip; sample 9802G displays a  $[c]$  axis maximum parallel to the lineation, suggesting prism  $[c]$  slip. Thermobarometry of these rocks implies peak metamorphic conditions of 800 °C, where prism  $[c]$  slip is active (McGrew *et al.* 2000). Most of the quartz CPOs are not representative of deformation at such high temperature (Lister *et al.* 1978; Schmid & Casey 1986), suggesting that they formed during cooling.

## CALCULATED VELOCITIES

### Funeral Mountains

The calculated velocities for each of the Funeral Mountain samples are shown in Fig. S12; the summary for the entire section is in Fig. 7. Samples MC1, MC2 and MC6, which have the least mica (8–10 volume per cent), are the least anisotropic (4–7 per cent). Some of the minerals in these two samples are strongly aligned, but the feldspar anisotropy and mica anisotropy counteract each other: the fast  $V_P$  directions of the feldspars are aligned with the slow  $V_P$  directions of the mica, reducing the rock anisotropy. Samples MC3 and MC5 display the greatest elastic anisotropy, with  $P$ - and  $S$ -wave anisotropy between 19 and 24 per cent. These two samples also have the most mica (40–50 per cent). The  $P$  and  $S$  anisotropy display uniaxial slow symmetry (or transverse isotropy) with the slow direction perpendicular to the foliation, as expected for mica-rich rock (Ji *et al.* 2002). Sample MC4 shows similar—though reduced—anisotropy. These three samples are characterized by random to weak quartz and feldspar CPOs and comparatively strong mica CPOs. The anisotropy magnitude is related to the amount of mica in the samples (~45 volume per cent mica in MC3 and MC5 versus 13 volume per cent mica in MC4).

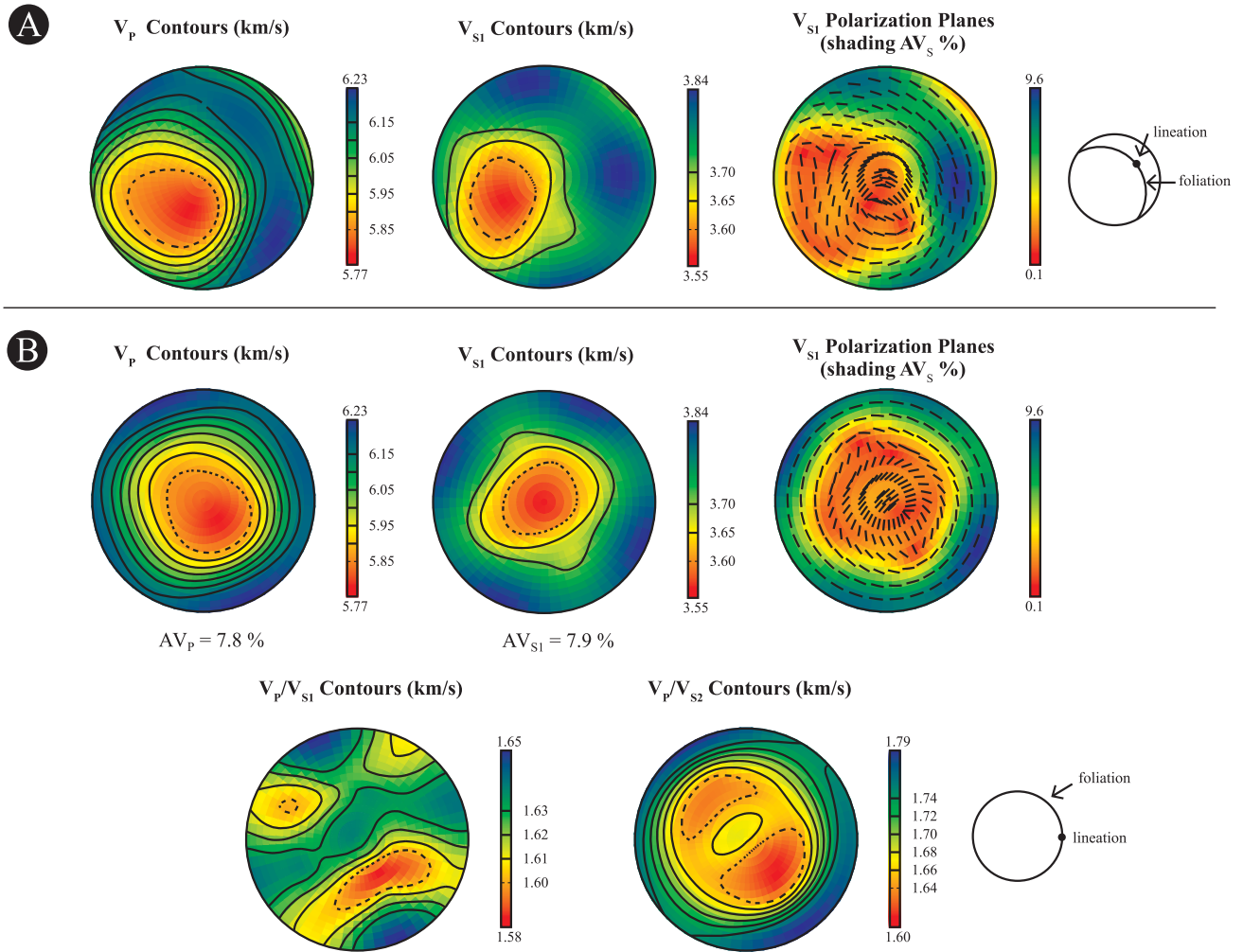


**Figure 7.** Acoustic properties for the Funeral Mountains section:  $V_p$ ,  $V_{S1}$ ,  $AV_S$ ,  $V_p/V_{S1}$  and  $V_p/V_{S2}$ . Lower hemisphere contour plots. (a) Geographic orientation. (b) Rotated such that the foliation is parallel to the page and the lineation is ‘east’.  $AV_p = (V_{Pmax} - V_{Pmin})/[(V_{Pmax} + V_{Pmin})/2] \times 100$ .  $AV_S = (V_{S1} - V_{S2})/[(V_{S1max} - V_{S1min})/2] \times 100$ ; polarization planes are shown with short line segments.

The velocities for the entire Funeral Mountains section (Fig. 7) were calculated without the much younger, discordant leucogranite; Table 1 shows that including the leucogranite in the calculations has essentially no effect on the absolute velocities, but reduces anisotropy by  $\sim 0.6$  percentage points ( $\sim 0.07$  percentage points per volume percent leucogranite). The  $V_p$  anisotropy,  $(V_{Pmax} - V_{Pmin})/[(V_{Pmax} + V_{Pmin})/2] \times 100$ , of the entire Monarch Canyon section is 7.8 per cent, with minimum and maximum  $V_p$  values of 5.8 and 6.2  $\text{km s}^{-1}$ ; the  $V_S$  anisotropy ranges from 0–9.6 per cent (0–0.35  $\text{km s}^{-1}$ ). The velocity anisotropy for the entire section has nearly uniaxial symmetry with a unique slow axis (transverse isotropy); the  $P$ -wave anisotropy can be characterized by an ellipse with axes of 1:1:0.94. The plane of fast directions is parallel to the foliation and the slow axis is perpendicular to the foliation. There is essentially no calculated  $S$ -wave splitting for waves propagating perpendicular to the foliation (i.e. arriving from a direction of  $\sim 45^\circ$ ,  $260^\circ$ ). The greatest  $S$ -wave splitting occurs for waves propagating along the foliation. Because the rocks in the Funeral Mountains have a significant dip, vertically incident shear waves will split slightly, allowing receiver functions to measure some anisotropy.

### Ruby Mountains

The velocity anisotropy of the Ruby Mountains sample suite is similar to that of the Funeral Mountains. The samples with the most mica (9804E, G and I) have the greatest anisotropy and display uniaxial symmetry with a unique slow axis for  $V_p$ , and minimal shear wave splitting for waves propagating perpendicular to the foliation (Fig. 8). Sample 9804I—the quartzofeldspathic gneiss—has the highest  $P$ - and  $S$ -wave anisotropy of the entire suite ( $AV_p = 12$  per cent,  $AV_S = 20$  per cent); samples 9804E and 9804G—the only calc-silicates with more than 15 volume per cent quartz—display slightly less  $P$ -wave and half the  $S$ -wave anisotropy ( $AV_p = \sim 8$  per cent,  $AV_S = \sim 10$  per cent). The strong anisotropy of sample 9804I is associated with a strong quartz CPO, a moderate plagioclase CPO and abundant mica. Sample 9804G is less anisotropic than 9804I because of a weak quartz CPO, and 9804E is less anisotropic despite a greater phyllosilicate abundance because of the destructive interference of the clinopyroxene and hornblende velocity anisotropies.

Other rocks in the Ruby Mountains suite (9804C, 9804D and 9804F) are less anisotropic: 2–5 per cent. These samples

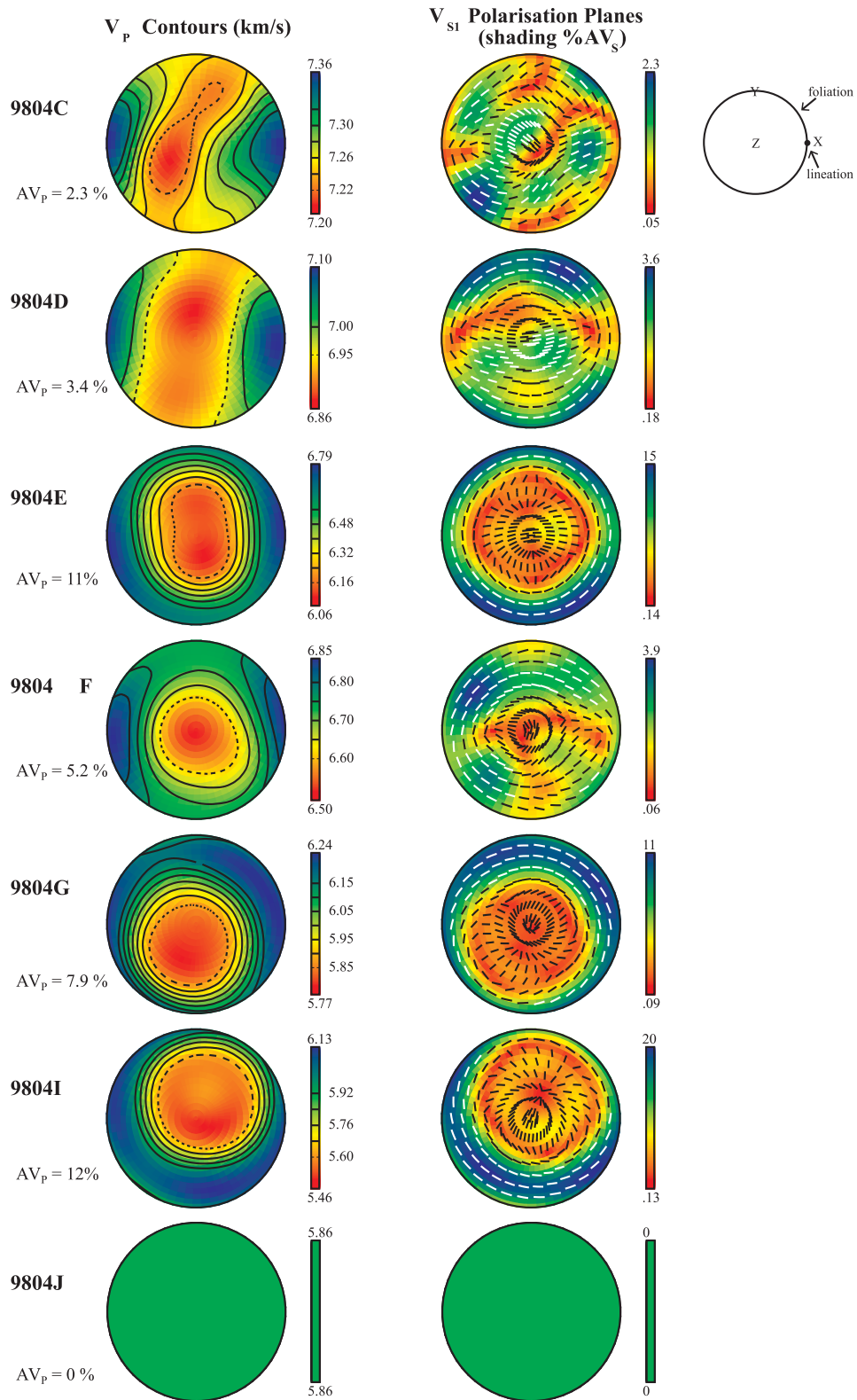


**Figure 8.** Lower hemisphere contour plots of  $V_P$  anisotropy and  $V_S$  anisotropy with  $V_{S1}$  polarization directions of Ruby Mountains samples. Top right figure shows the orientation of the plots;  $X$  is the lineation,  $Y$  is perpendicular to the lineation and  $Z$  is normal to the foliation.

contain calcite and dolomite, large amounts of clinopyroxene and few phyllosilicates.  $P$ -wave and shear wave splitting anisotropies are typically not correlated; the  $P$ -wave anisotropies have orthorhombic symmetry whereas the  $S$ -wave anisotropies have lower sym-

metry. The low anisotropy is attributable to low phyllosilicate abundance, random calcite and dolomite CPOs ( $MUD < 1.8$ ), and weak to moderate plagioclase CPOs ( $MUD < 3$ ). Because it is massive and equigranular—and therefore expected to be

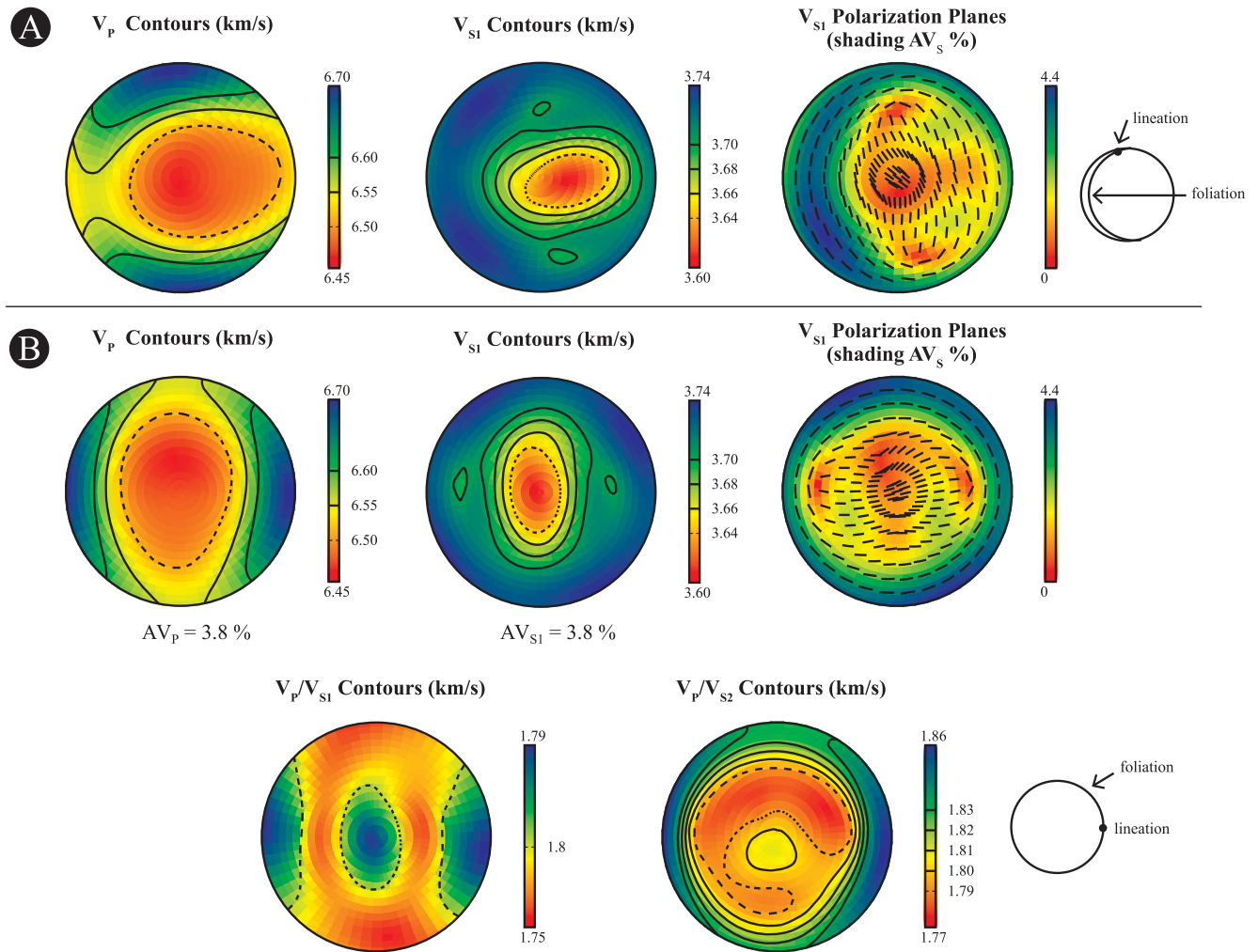


**Figure 9.** Acoustic properties for the Ruby Mountains section:  $V_p$ ,  $V_{S1}$ ,  $AV_s$ ,  $V_p/V_{S1}$  and  $V_p/V_{S2}$ . Lower hemisphere contour plots. (a) Geographic orientation. (b) Rotated such that the foliation is parallel to the page and the lineation is ‘east’.

elastically isotropic—the velocity of leucogranite 9804J was reduced to a scalar.

The velocity for the entire Ruby Mountains section (Fig. 9) is distinctly different than that of the Funeral Mountains. The velocities are faster ( $V_p = 6.4\text{--}6.7\text{ km s}^{-1}$ ), but the anisotropy is lower ( $V_p$  anisotropy = 3.8 per cent;  $V_s$  anisotropy = 0.2–4.4 per cent). Rather than the uniaxial anisotropy of the Funeral Mountains, the  $V_p$  anisotropy of the Ruby Mountains has orthorhombic symmetry, with the fast direction parallel to the lineation and the slow direction perpendicular to the foliation; it can be described by an ellipsoid with axes of 1.02:1:0.99. Like the Funeral Mountains, the shear wave splitting is greatest for waves propagating along the foliation, and nearly zero for waves propagating perpendicular to the foliation. (Because the leucogranite 9804J is discordant and post-dates the peak metamorphism (summary in Howard 2003), these calculations were done both with and without the leucogranite; Table 1.)

### East Humboldt Range

The velocity anisotropy of the EHR samples is similar to the Funeral Mountains samples (Figs S13 and S14). For example, the sample (9803H) with the greatest anisotropy ( $AV_p = 14$  per cent,  $AV_s = 19$  per cent) has the most mica, and shows uniaxial symmetry with the

unique slow axis perpendicular to the foliation. However, in other ways the two regions are different. The EHR samples with fairly high anisotropy—10–16 per cent  $AV_p$  or  $AV_s$ —have no more than 6 volume per cent mica (9802B, 9803B and 9803G). Instead, they all have >85 volume per cent quartz with a strong CPO (MUD 10–14). The  $P$ -wave velocity anisotropy for these three samples typically has a unique fast direction perpendicular to the lineation and a slow plane parallel to the lineation and perpendicular to the foliation; the  $S$ -wave anisotropy has lower symmetry. Sample 9803B differs slightly in that the velocity anisotropy is more complicated, with a uniaxial slow component related to its higher mica content. Other quartzofeldspathic rocks in the EHR typically have moderate anisotropy:  $P$ -wave anisotropy between 2 and 7 per cent and shear wave splitting of 5–8 per cent. These rocks have asymmetric quartz CPOs and weak to moderate CPOs for plagioclase and K-feldspar (MUD  $\sim 2\text{--}5$ ). Compared to the Ruby Mountains, the marble sample from the EHR (9802E) has strong anisotropy: 9 per cent for  $P$  waves and 7 per cent shear wave splitting. In this sample, the major minerals, calcite and dolomite, have strong CPOs (MUD = 5), with their slow directions perpendicular to the foliation. The two calc-silicates (9802C and 9803E) have moderate anisotropy— $AV_p = 5$  per cent and  $AV_s = 4$  per cent—and are characterized by weak to moderate CPOs and no mica. Sample 9802G—a quartzofeldspathic

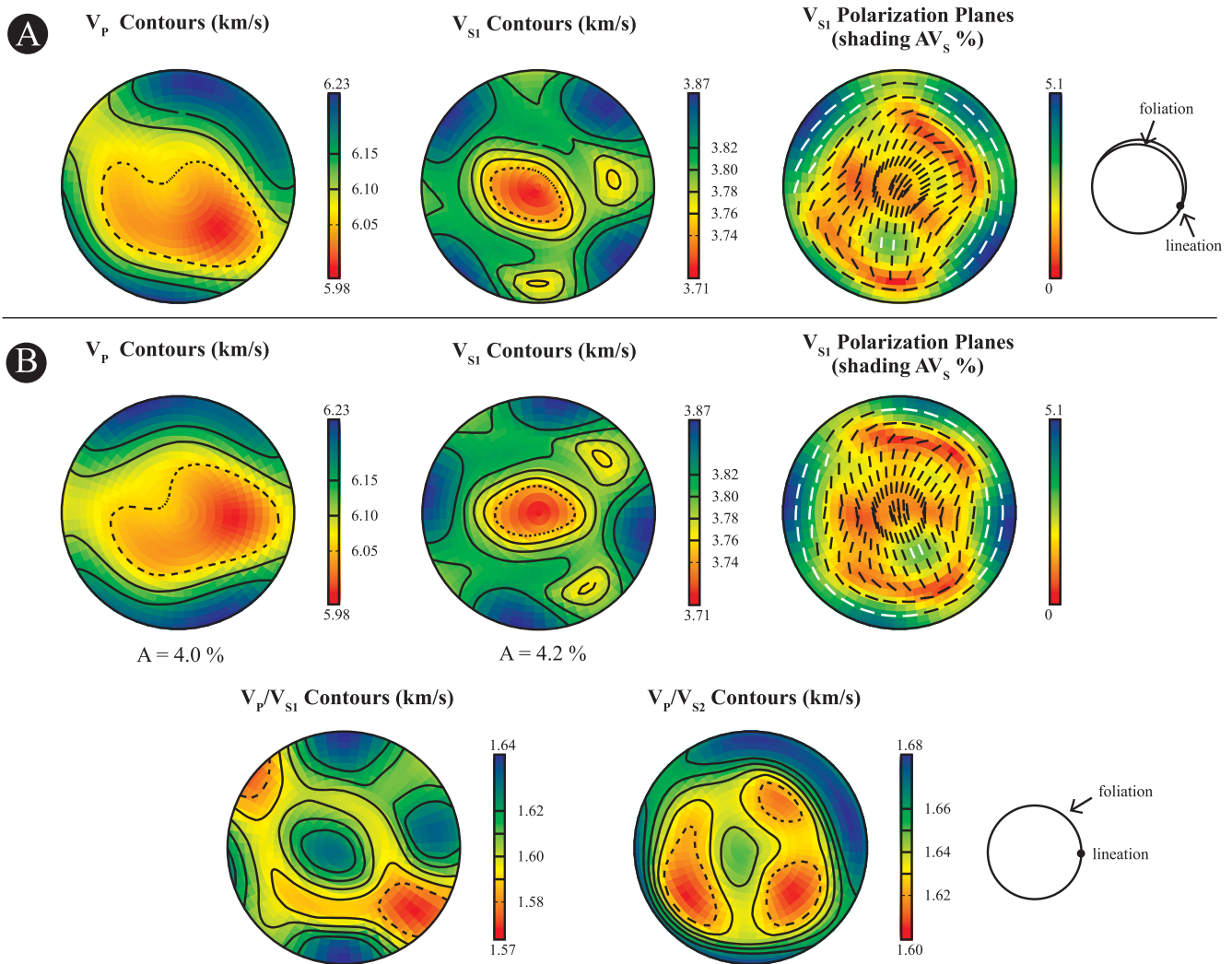


**Figure 10.** Acoustic properties for the East Humboldt Range section:  $V_p$ ,  $V_{s1}$ ,  $AV_s$ ,  $V_p/V_{s1}$  and  $V_p/V_{s2}$ . Lower hemisphere contour plots. (a) Geographic orientation. (b) Rotated such that the foliation is parallel to the page and the lineation is ‘east’.

gneiss—has the lowest anisotropy of the section:  $AV_p = 2$  per cent and  $AV_s = 5$  per cent. This sample is characterized by a quartz CPO indicative of basal (a) slip and weak to moderate plagioclase and K-feldspar CPOs (MUD = 3–4).

The velocity for the entire EHR section (Fig. 10) was computed by combining the Angel Lake (sample names beginning with 9802) and Lizzie’s Basin (sample names beginning with 9803) sites in equal proportions. The bulk  $V_p$  anisotropy is 4.0 per cent, with  $V_p$  ranging from 6.0–6.2  $\text{km s}^{-1}$ ; the bulk shear wave anisotropy ranges from 0.13–5.12 per cent (0–0.19  $\text{km s}^{-1}$ ). The  $V_p$  anisotropy has orthorhombic symmetry (transverse anisotropy) with the fast direction perpendicular to the lineation and the slow direction sub-perpendicular to the foliation.  $AV_p$  can be described by an ellipsoid with axes of 1:1.02:0.97. The shear wave splitting also displays orthorhombic symmetry, with the least splitting for waves propagating perpendicular to the foliation, and the most splitting for waves propagating parallel to the lineation. Similar to the Funeral Mountains and Ruby Mountains sections, and typical of the lower crust in this tectonic setting, no shear wave splitting is predicted in the EHR for waves propagating at  $\sim 0$ – $45^\circ$  from the vertical. However, the orthorhombic symmetry of both the  $P$ - and  $S$ -wave anisotropies could permit a fast direction to be determined from horizontally incident

body waves. The low mica content of this sample suite confirms that the Basin and Range mid- to lower crust is not homogeneous with respect to mica content. Because the discordant igneous rocks (9802D and 9802J and 9803C) post-date the peak metamorphism (Snoke *et al.* 1997) the velocity calculations were done both with and without the igneous rocks (Table 1).

## DISCUSSION

If the mineralogies and CPOs of the rocks measured in this study are typical of the middle to lower crust, the calculated velocities of the three studied sections should be representative of quartzofeldspathic lower crust in general. We can then use these data and calculations to address several questions—with the caveat that the answers reflect this dataset only.

(1) Can the absolute velocity of seismic waves be used to infer lower crustal mineralogy?

Earth’s continental crust is typically subdivided into two or three discrete layers on the basis of seismic velocities (Smithson 1978; Holbrook *et al.* 1992). The measured  $P$ -wave velocity of the middle crust and lower crust—extrapolated to room temperature and 600

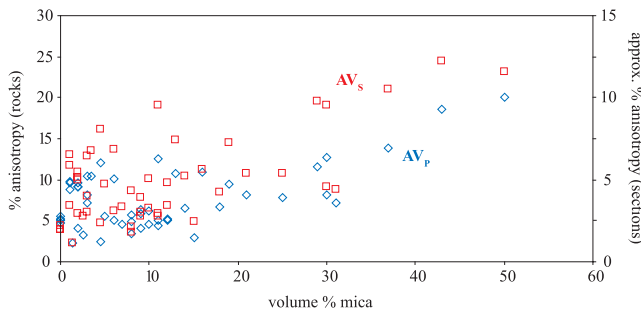


**Figure 11.** Velocity anisotropy is correlated with mica abundance. Percent anisotropy of individual rocks is typically twice that of crustal sections.

MPa—is typically 6.4–6.7 and 6.7–7.1 km s<sup>-1</sup>, respectively (Christensen & Mooney 1995; Rudnick & Fountain 1995). Numerous studies have shown that absolute velocities alone are not a good discriminant for bulk composition or mineralogy (Pakiser & Robinson 1966; Reid *et al.* 1989; Holbrook *et al.* 1992; Rudnick & Fountain 1995; Behn & Kelemen 2003). This conclusion is supported by the calculations in Table 1. On average, the three sections measured in this study have velocities typical of those reported for the middle crust, but the clinopyroxene-bearing calc-silicate rocks have velocities typical of the lower crust. All of these rocks are typical of the miogeoclinal sections of western North American core complexes, and all were exhumed from the same depths—velocity cannot be used to separate the rocks into ‘middle’ and ‘lower’ crustal rocks.

(2) Can the velocity *anisotropy* measured by seismic waves be used to infer lower crustal mineralogy?

Velocity anisotropy can be used to infer mineralogy only in combination with  $V_p/V_s$ , and only then with some additional assumptions. In this study, the magnitude of anisotropy is correlated with the abundance of mica in rocks with >12 volume per cent mica (Fig. 11); rocks with less mica generally are not as anisotropic. Amphibolites have been suggested to be major contributors to anisotropy in high-velocity crustal sections, but amphibolites are generally less anisotropic (Barruol & Kern 1996; Weiss *et al.* 1999; Tatham *et al.* 2008; Kono *et al.* 2009), like the clinopyroxene-rich samples from the Ruby Mountains. It would be prudent to combine measures of absolute velocity and  $V_p/V_s$  with anisotropy to discriminate between mica- and amphibole-dominated sections.

Previous studies using methods similar to this study have demonstrated that micaceous rocks have strong velocity anisotropy (e.g. Weiss *et al.* 1999; Meltzer & Christensen 2001; Mahan 2006; Valcke *et al.* 2006; Barberini *et al.* 2007; Lloyd *et al.* 2009; Ward *et al.* 2012). The anisotropies reported in this study for individual samples are slightly higher than those reported in previous studies.  $P$ -wave anisotropy in this study ranges from 0–20 per cent with an average of 7 per cent, whereas other studies report 0–16 per cent, and an average of 7 per cent. In this study  $S$ -wave anisotropy ranges from 0–25 per cent with an average of 9 per cent, whereas previous studies report 0–25 per cent, and an average of 6 per cent (Fig. 12a). For individual samples  $AV_s$  is typically 25 per cent higher than  $AV_p$  in this study, whereas previous studies typically report  $AV_p$  that is twice as large as  $AV_s$ . In part this difference may be because many previous studies did not measure the CPO of all minerals in some rocks. Additionally, the anisotropies reported here are for rocks rich in biotite and muscovite, for which  $AV_s$  is 26 per cent and 78 per cent greater than  $AV_p$ , respectively. Only three of the samples ( $N = 41$ ) in previous studies have a mica composition above 15 volume percent. Thus, large-magnitude crustal seismic anisotropy is almost certainly a signature of micaceous rock.

(3) Can the velocity anisotropy of individual samples be generalized to the scale at which seismic waves sample the mid–lower crust?

The answer to this question depends on many factors—such as mineralogy, strain geometry, CPO strength, thickness of layering, folding, rock fabric (Weiss *et al.* 1999; Meissner *et al.* 2006; Lloyd *et al.* 2009)—such that the question might best be addressed by simply looking at what has been reported by studies of various crustal sections (Fig. 12b). These studies show that the median  $V_p$  anisotropy reported for individual samples is ~6 per cent, whereas the median  $V_p$  anisotropy reported for studied crustal sections is ~4 per cent. The median  $V_s$  anisotropy reported for individual samples is ~7 per cent (this study) or 4 per cent (other studies), whereas the median  $V_s$  anisotropy reported for studied crustal sections is ~3.5 per cent. Layering contributes less to acoustic anisotropy than CPOs (Weiss *et al.* 1999).

Bulk  $AV_p$  values calculated for the Ivrea Zone, Italy, average 5 per cent and  $AV_s$  averages 3 per cent over 7 km of palaeovertical section (Barruol & Kern 1996; Weiss *et al.* 1999). The Ruby Mountains and EHR calculated bulk velocities are similar for ~1 km of palaeovertical section (Fig. 12b), whereas the calculated bulk anisotropy for the Funeral Mountains is towards the high end of the range. The relatively high anisotropy calculated for the Funeral Mountains reflects the abundance of mica in the analysed samples and the relative homogeneity of the section. In summary, the calculated anisotropies for crustal sections are typically about half that observed in individual samples of common rocks.

(4) Can velocity anisotropy be used to infer lower crustal flow?

Yes, but only the flow *plane* and *not the flow direction*. All three studied sections show that waves propagating perpendicular to the rock flow plane are the slowest and show the least  $S$ -wave splitting. Determining the flow *direction* in crustal rocks purely from velocity anisotropy is problematic for this particular dataset. In the Funeral Mountains, the velocity anisotropy is near-uniaxial, with equivalent velocities for waves propagating in all directions in the flow plane. In the Ruby Mountains, the fast  $P$ -wave direction is parallel to the flow direction, whereas in the EHR, the fast direction is perpendicular to the flow direction. Similar, nonsystematic weak deviations from transverse isotropy have been reported for other crustal sections (e.g. Weiss *et al.* 1999).

(5) Can  $V_p/V_s$  be used to infer lower crustal mineralogy?

Christensen (1996) noted that rocks with SiO<sub>2</sub> contents of 55–100 per cent have predictable  $V_p/V_s$  ratios because of the dramatically low  $V_p/V_s$  ratio for alpha quartz. He presented a quantitative and precise relationship (although note that the quadratic fit presented in that paper has a sign error; the ‘-’ should be ‘+’). The inverse of this—using  $V_p/V_s$  ratios to infer SiO<sub>2</sub> content in this range—was championed, and has been extensively used (e.g. Hauser *et al.* 2008). The accuracy of this relationship is overstated, however.

(1) Inspection of Fig. 13 in Christensen (1996) shows that one can only infer SiO<sub>2</sub> content if  $V_p/V_s < 1.74$  (Poisson’s ratio,  $\sigma < 0.25$ ). This limitation exists because a variety of low-silica rocks have no quartz, but they have another mineral—such as orthopyroxene—that diminishes  $V_p/V_s$ . This relationship fits the *isotropic*  $V_p/V_s$  values measured in this study (black symbols in Fig. 13).

(2) Anisotropy plays a role. Because the velocities for all the rocks and crustal sections in this study are anisotropic, the *isotropic* value is not an accurate representation of the average velocity sampled by seismic waves. A more accurate representation is given by the blue symbols in Fig. 13, which represent the velocity ratios averaged over all directions. Note that the SiO<sub>2</sub> content inferred

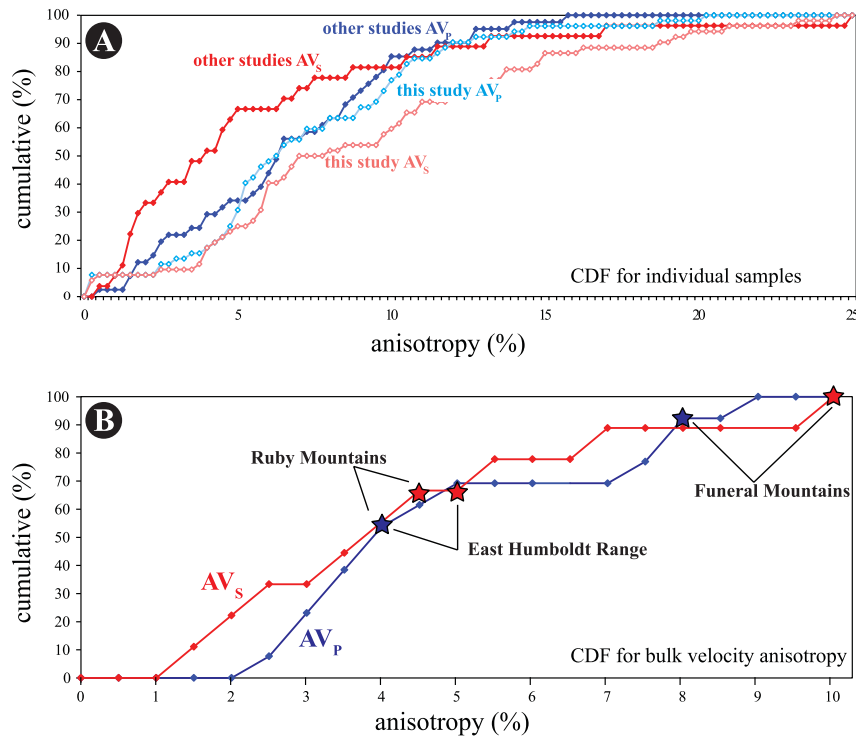


**Figure 12.** Cumulative distributions of (a) individual rock sample velocity anisotropy and (b) velocity anisotropy for crustal sections. Stars in (b) indicate values derived from this study. Data from other studies were compiled from Barruol & Kern (1996), Weiss *et al.* (1999), Burlini *et al.* (2005), Barberini *et al.* (2007), Kern *et al.* (2008), Tatham *et al.* (2008), Lloyd *et al.* (2009), Kono *et al.* (2009) and Lloyd *et al.* (2010).

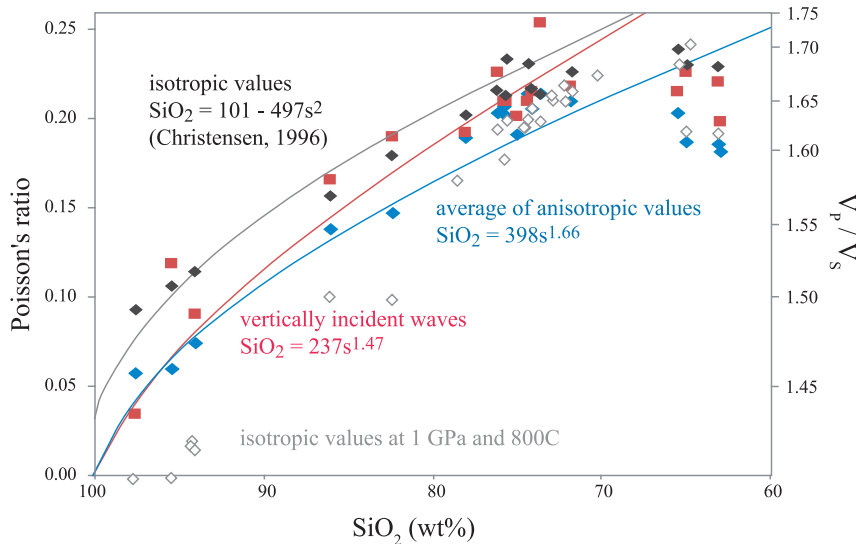


**Figure 13.** Relationship between  $V_p/V_s$  or Poisson's ratio ( $\sigma$ ) and silica content of crustal rocks in this study. Isotropic ratios (calculated from the elastic moduli and density) are highest and are well characterized by the (corrected) equation of Christensen (1996). The average ratios—computed as the geometric mean of the velocity ratio in all directions sampled over  $1^\circ$  intervals—is lower. The ratios for vertically incident waves—computed as the mean of the velocity ratio for waves propagating orthogonal to the foliation sampled over  $1^\circ$  intervals—is intermediate. Relationships break down beyond  $\sigma = 0.25$  and cannot be used (see text).

from these values differs from the Christensen (1996) relationship by  $>5$  wt. per cent—or  $>0.04$   $\sigma$ —depending on whether you prefer to think in terms of crustal composition or velocity. If strong anisotropy exists, it will be difficult to get an accurate or useful  $V_p/V_s$  measurement.

(3) Anisotropy plays a second role when the foliation in the crustal section has a specific orientation with respect to the wave

propagation direction. In crustal sections where the foliation is subhorizontal—like this study—vertically propagating waves ‘see’ higher  $V_p/V_s$  ratios than the average and are shown in red in Fig. 13.

(4) Because the relationship between  $V_p/V_s$  and  $\text{SiO}_2$  content is principally due to the presence of quartz, changes in the elastic properties of quartz affect this relationship dramatically. For example, whereas the Poisson's ratio for alpha quartz is 0.08 at STP, it

is  $-0.05$  at 1 GPa and  $800\text{ }^{\circ}\text{C}$  (Hacker & Abers 2004), leading to significant decreases in rock  $V_P/V_S$  shown in grey in Fig. 13. At 1 GPa and  $850\text{ }^{\circ}\text{C}$ , where beta quartz is stable, Poisson's ratio in quartz is 0.22, and the ratios increase dramatically upward.

In aggregate, these considerations mean that the use of  $V_P/V_S$  to assess the  $\text{SiO}_2$  content of Earth's crust should be limited to  $V_P/V_S < 1.74$ . At STP, this relationship has an accuracy of  $\sim 5$  wt. per cent  $\text{SiO}_2$  because of the anisotropy inherent in crustal sections, and the inaccuracy will be larger at depth unless the ambient pressure and temperature are well known.

## CONCLUSIONS

Agreement between measured and calculated velocities shows that seismic velocities calculated from mineral CPOs and elastic constants are representative of actual rock properties. Calculating velocities from CPOs measured via EBSD provides advantages over the PT technique in that measurements are not affected by the presence of cracks, alteration, and low-pressure phases. That is to say, the effects of exhumation can be eliminated and the properties of a rock in its original crack-free, alteration-free, high-pressure and high-temperature condition can be calculated.

Samples from the Funeral Mountains, Ruby Mountains and EHR measured by EBSD demonstrate that seismic anisotropy varies across the Basin and Range because of changes in mineralogy and strain. The slow  $P$ - and  $S$ -wave propagation directions are normal to the foliation in all three sections, and the velocity anisotropy shows either transverse isotropy or nearly so. This means little to no shear wave splitting for near-vertically incident body waves transmitted through crustal rocks with a subhorizontal foliation. As a result, such locations are good places to measure mantle anisotropy because crustal anisotropy is minimal in the vertical direction. Velocity anisotropy can be used to infer the flow plane, but not the flow direction in typical crustal rocks: the Funeral Mountains has uniaxial symmetry/transverse isotropy, and although the Ruby Mountains and EHR have orthorhombic symmetry, the flow direction is marked by the fast axis in one mountain range and by the intermediate axis in the other mountain range.

## ACKNOWLEDGEMENTS

Funded by NSF grants EAR-0649933 and EAR-0745620. Barbara John graciously provided the McDonough & Fountain (1993) samples. Special thanks to Sarah Brownlee for providing the Matlab script to integrate EDS and EBSD data and to Allen McGrew for his geological maps of the Ruby–EHR area. Marty Giaramita, Keith Howard, Chris Mattinson, Allen McGrew, and Art Snoke gave helpful advice regarding Basin and Range geology.

## REFERENCES

- Aleksandrov, K.S. & Ryzhova, T.V., 1961. The elastic properties of rock-forming minerals II: layered silicates, *Bull. Acad. Sci. U.S.S.R., Geophys. Ser.*, **9**, 1165–1168.
- Aleksandrov, K.S., Alchikov, V.V., Belikov, B.P., Zaslavskii, B.I. & Krupnyi, A.I., 1974. Velocities of elastic waves in minerals at atmospheric pressure and increasing precision of elastic constants by means of EVM (in Russian), *Bull. Acad. Sci. U.S.S.R., Geol. Ser.*, **10**, 15–24.
- Aplegate, J.D.R. & Hodges, K.V., 1995. Mesozoic and Cenozoic extension recorded by metamorphic rocks in the Funeral Mountains, California, *Geol. Soc. Am. Bull.*, **107**(9), 1063–1076.
- Babuska, V., Fiala, J., Kumazawa, M., Ohno, I. & Sumino, Y., 1978. Elastic properties of garnet solid solution series, *Phys. Earth planet. Inter.*, **16**, 157–176.
- Barberini, V., Burlini, L. & Zappone, A., 2007. Elastic properties, fabric and seismic anisotropy of amphibolites and their contribution to the lower crust reflectivity, *Tectonophysics*, **445**, 227–244.
- Barruol, G. & Kern, H., 1996. Seismic anisotropy and shear-wave splitting in lower-crustal and upper-mantle rocks from the Ivrea Zone: experimental and calculated data, *Phys. Earth planet. Inter.*, **95**(3–4), 175–194.
- Barth, N.C., Hacker, B.R., Seward, G.G.E., Walsh, E.O., Young, D. & Johnston, S., 2010. Strain within the ultrahigh-pressure Western Gneiss region of Norway recorded by quartz CPOs, in *Continental Tectonics and Mountain Building: The Legacy of Peach and Horne*, Vol. 335, pp. 663–685, eds Law, R.D., Butler, R.W.H., Holdsworth, R.E., Krabbendam, M. & Strachan, R.A., Geological Society Special Publications.
- Bass, J.D., 1995. Elasticity of minerals, glasses, and melts, in *Mineral Physics and Crystallography: A Handbook of Physical Constants*, Vol. 2, pp. 45–63, ed. Ahrens, T.J., *AGU Ref. Shelf*, AGU.
- Behn, M.D. & Kelemen, P.B., 2003. Relationship between seismic P-wave velocity and the composition of anhydrous igneous and meta-igneous rocks, *G-cubed*, **4**, article 1041.
- Belikov, B.P., Aleksandrov, K.S. & Ryzhova, T.V., 1970. *Elastic Properties of Rock-forming Minerals and Rocks*, Nauka Press.
- Birch, F., 1960. The velocity of compressional waves in rocks to 10 kilobars, Part 21, published under the auspices of the Committee on Experimental Geology and Geophysics and the Department of Geological Sciences at Harvard University, *J. geophys. Res.*, **66**(7), 2199–2224.
- Brown, J.M., Abramson, E.H. & Angel, R.J., 2007. Triclinic elastic constants for low albite, *Phys. Chem. Miner.*, **33**(4), 256–265.
- Brownlee, S.J., Hacker, B.R., Salisbury, M., Seward, G., Little, T., Baldwin, S. & Abers, G.A., 2011. Predicted velocity and density structure of the exhuming Papua New Guinea ultrahigh-pressure terrane, *J. geophys. Res.*, **116**, B08206, doi:10.1029/2011JB008195.
- Burlini, L. & Fountain, D.M., 1993. Seismic anisotropy of metapelites from the Ivrea-Verbano zone and Serie dei Laghi (northern Italy), *Phys. Earth planet. Inter.*, **78**, 301–317.
- Burlini, L., Arbaret, L., Zeilinger, G. & Burg, J.-P., 2005. High-temperature and pressure seismic properties of a lower crustal prograde shear zone from the Kohistan Arc, Pakistan, in *High-Strain Zones: Structure and Physical Properties*, Vol. 245, pp. 187–202, eds Bruhn, D. & Burlini, L., Geological Society Special Publications.
- Burlini, L., Marquer, D., Challandes, N., Mazzola, S. & Zangarini, N., 1998. Seismic properties of highly strained marbles from the Spluegenpass, Central Alps, *J. Struct. Geol.*, **20**(2–3), 277–292.
- Christensen, N.I., 1965. Compressional wave velocities in metamorphic rocks at pressures to 10 kilobars, *J. geophys. Res.*, **70**, 6147–6166.
- Christensen, N.I., 1984. The magnitude, symmetry, and origin of upper mantle anisotropy based on fabric analyses of ultramafic tectonites, *Geophys. J. R. Astr. Soc.*, **76**, 89–111.
- Christensen, N.I., 1996. Poisson's ratio and crustal seismology, *J. geophys. Res.*, **101**(B2), 3139–3156.
- Christensen, N.I. & Mooney, W.D., 1995. Seismic velocity structure and composition of the continental crust: a global view, *J. Geophys. Res.*, **100**, 9761–9788.
- Collins, M.D. & Brown, J.M., 1998. Elasticity of an upper mantle clinopyroxene, *Phys. Chem. Miner.*, **26**, 7–13.
- Coney, P.J. & Harms, T.A., 1984. Cordilleran metamorphic core complexes: Cenozoic extensional relics of Mesozoic compression, *Geology*, **12**, 550–554.
- Crosson, R.S. & Lin, J.W., 1971. Voigt and Reuss prediction of anisotropic elasticity of dunite, *Res. Lett.*, **76**(6), 570–578.
- Currie, C.A., Cassidy, J.F., Hyndman, R.D. & Bostock, M.G., 2004. Shear wave anisotropy beneath the Cascadia subduction zone and western North American craton, *Geophys. J. Int.*, **157**, 341–353.
- Dandekar, D.P., 1968. Variation of the elastic constants of calcite with temperature, *J. appl. Phys.*, **39**, 3694–3699.
- Godfrey, N.J., Christensen, N.I. & Okaya, D.A., 2000. Anisotropy of schists: contribution of crustal anisotropy to active source seismic experiments

- and shear wave splitting observations, *J. geophys. Res.*, **105**(B12), 27 991–28 007.
- Hacker, B.R. & Abers, G.A., 2004. Subduction Factory 3: an Excel Worksheet and Macro for calculating the densities, seismic wave speeds, and H<sub>2</sub>O contents of minerals and rocks at pressure and temperature, *Geochem., Geophys., Geosyst.*, **5**(1), Q01005, doi:10.1029/2003GC000614.
- Hacker, B.R. & Abers, G.A., 2012. Subduction Factory 5. Unusually low Poisson's ratios in subduction zones from elastic anisotropy of peridotite, *J. Geophys. Res.*, **117**, B06308, doi:10.1029/2012JB009187.
- Hasbrouck, W.P., 1964. A seismic reflection crustal study in central eastern Colorado, *PhD thesis*, Colorado School of Mines, Golden, CO.
- Hauser, F., O'Reilly, B.M., Readman, P.W., Daly, J.S. & van den Berg, R., 2008. Constraints on crustal structure and composition within a continental suture zone in the Irish Caledonides from shear wave wide-angle reflection data and lower crustal xenoliths, *Geophys. J. Int.*, **175**(3), 1254–1272.
- Hearmon, R.F.S., 1984. The elastic constants of crystals and other anisotropic materials, in *Landolt-Bornstein Tables, III/18*, pp. 1–154, eds Hellwege, K.H. & Hellwege, A.M., Springer-Verlag.
- Hearn, T.M., 1996. Anisotropic Pn tomography in the western United States, *J. geophys. Res.*, **101**(B4), 8403–8414.
- Hodges, K.V. & Walker, J.D., 1990. Petrologic constraints on the unroofing history of the Funeral Mountains Metamorphic Core Complex, California, *J. geophys. Res.*, **95**, 8437–8445.
- Hodges, K.V., Snoke, A.W. & Hurlow, H.A., 1992. Thermal evolution of a portion of the Sevier hinterland: the northern Ruby Mountains–East Humboldt Range and Wood Hills, northeastern Nevada, *Tectonics*, **11**(1), 154–164.
- Holbrook, W.S., Mooney, W.D. & Christensen, N.I., 1992. The seismic velocity structure of the deep continental crust, in *Continental lower crust, Developments in Geotectonics*, pp. 1–42, eds Fountain, D.M., Arculus, R. & Kay, R.W., Elsevier.
- Howard, K.A., 2003. Crustal structure in the Elko–Carlin Region, Nevada, during Eocene gold mineralization: Ruby–East Humboldt metamorphic core complex as a guide to the deep crust, *Econ. Geol. Bull. Soc. Econ. Geol.*, **98**(2), 249–268.
- Hudec, M.R., 1992. Mesozoic structural and metamorphic history of the central Ruby Mountains metamorphic core complex, Nevada, *Geol. Soc. Am. Bull.*, **104**, 1086–1100.
- Humbert, P. & Plique, F., 1972. Propriétés élastiques de carbonates rhomboédriques monocristallins calcite, magnésite, dolomite, *C.R. Acad. Sci. Paris*, **275**, B391–B394.
- Ivankina, T.I., Kern, H.M. & Nikitin, A.N., 2005. Directional dependence of P- and S-wave propagation and polarization in foliated rocks from the Kola superdeep well: evidence from laboratory measurements and calculations based on TOF neutron diffraction, *Tectonophysics*, **407**, 25–42.
- Ji, S., Salisbury, M.H. & Hanmer, S., 1993. Petrofabric, P-wave anisotropy and seismic reflectivity of high-grade tectonites, *Tectonophysics*, **222**(2), 195–226.
- Ji, S., Wang, Q. & Xia, B., 2002. *Handbook of Seismic Properties of Minerals, Rocks, and Ores*, Polytechnic International Press.
- Karato, S., Jung, H., Katayama, I. & Skemer, P., 2008. Geodynamic significance of seismic anisotropy of the upper mantle: new insights from laboratory studies, *Ann. Rev. Earth planet. Stud.*, **36**, 59–95.
- Kern, H., Ivankina, T.I., Nikitin, A.N., Lokajicek, T. & Pros, Z., 2008. The effect of oriented microcracks and crystallographic and shape preferred orientation on bulk elastic anisotropy of a foliated biotite gneiss from Outokumpu, *Tectonophysics*, **457**, 143–149.
- Kono, Y., Ishikawa, M., Yumiko, H., Katsuyoshi, M. & Makoto, A., 2009. P- and S-wave velocities of the lowermost crustal rocks from the Kohistan arc: Implications for seismic Moho discontinuity attributed to abundant garnet, *Tectonophysics*, **467**, 44–54.
- Lloyd, G., Law, R.D. & Mainprice, D., 2010. Predicting seismic properties from three-dimensional microstructures: a new look at an old quartzite, in *Continental Tectonics and Mountain Building: The Legacy of Peach and Horne*, Vol. 335, pp. 601–620, eds Law, R.D., Butler, R.W.H., Holdsworth, R.E., Krabbendam, M. & Strachan, R.A., Geological Society Special Publications.
- Lloyd, G., Butler, R.W.H., Casey, M. & Mainprice, D., 2009. Mica, deformation fabrics and the seismic properties of the continental crust, *Earth planet. Sci. Lett.*, **228**, 320–328.
- Long, M.D. & Silver, P.G., 2008. The subduction zone flow field from seismic anisotropy: a global view, *Science*, **319**, 315–318.
- Long, M.D. & Silver, P.G., 2009. Mantle flow in subduction systems: The slab flow field and implications for mantle dynamics, *J. geophys. Res.*, **114**, B10312, doi:10.1029/2008JB006200.
- Lakshmanov, D.L., Sinogeikin, S.V. & Bass, J.D., 2007. High-temperature phase transitions and elasticity of silica polymorphs, *Phys. Chem. Miner.*, **34**, 11–22.
- Lister, G.S. & Hobbs, B.E., 1980. The simulation of fabric development during plastic deformation and its application to quartzite: the influence of deformation history, *J. Struct. Geol.*, **2**(3), 355–370.
- Lister, G.S., Paterson, M.S. & Hobbs, B.E., 1978. The simulation of fabric development in plastic deformation and its application to quartzite: the model, *Tectonophysics*, **45**, 107–158.
- Mahan, K., 2006. Retrograde mica in deep crustal granulites: implications for crustal seismic anisotropy, *Geophys. Res. Lett.*, **33**, L24301, doi:10.1029/2006GL028130.
- Mainprice, D., 1990. A FORTRAN program to calculate seismic anisotropy from the lattice preferred orientation of minerals, *Comput. Geosci.*, **16**, 385–393.
- Mainprice, D. & Nicolas, A., 1989. Development of shape and lattice preferred orientations: application to the seismic anisotropy of the lower crust, *J. Struct. Geol.*, **11**, 175–189.
- Mao, Z., Fuming, J. & Duffy, T.S., 2007. Single-crystal elasticity of zoisite Ca<sub>2</sub>Al<sub>3</sub>Si<sub>3</sub>O<sub>12</sub>(OH) by Brillouin scattering, *Am. Mineral.*, **92**, 570–576.
- Mattinson, C.G., Colgan, J.P., Metcalf, J.R., Miller, E.L. & Wooden, J.L., 2007. Late Cretaceous to Paleocene metamorphism and magmatism in the Funeral Mountains metamorphic core complex, Death Valley, California, in *Convergent Margin Terranes and Associated Regions: A Tribute to W. G. Ernst*, Vol. 419, pp. 205–223, eds Cloos, M., Carlson, W.D., Gilbert, M.C., Liou, J.G. & Sorensen, S.S., Geological Society of America Special Paper.
- McDonough, D.T. & Fountain, D.M., 1993. P-wave anisotropy of mylonitic and infrastructural rocks from a Cordilleran core complex: the Ruby–East Humboldt Range, Nevada, *Phys. Earth planet. Inter.*, **78**(3–4), 319–336.
- McGrew, A.J., Peters, M.T. & Wright, J.E., 2000. Thermobarometric constraints on the tectonothermal evolution of the East Humboldt Range metamorphic core complex, Nevada, *Geol. Soc. Am. Bull.*, **112**, 45–60.
- McNamara, D. & Owens, T., 1993. Azimuthal shear wave velocity anisotropy in the Basin and Range province using Moho Ps converted phases, *J. geophys. Res.*, **98**(B7), 12 003–12 017.
- Meissner, R., Rabbal, W. & Kern, H., 2006. Seismic lamination and anisotropy of the lower continental crust, *Tectonophysics*, **416**, 81–99.
- Mehl, L., Hacker, B.R. & Hirth, G., 2003. Arc-parallel flow within the mantle wedge: evidence from the accreted Talkeetna arc, south central Alaska, *J. geophys. Res.*, **108**(B8), 2375, doi:10.1029/2002JB002233.
- Meltzer, A. & Christensen, N., 2001. Nanga Parbat crustal anisotropy: implications for interpretation of crustal velocity structure and shear-wave splitting, *Geophys. Res. Lett.*, **28**(10), 2129–2132.
- Moschetti, M.P., 2010. Seismic evidence for widespread western-US deep-crustal deformation caused by extension, *Nature*, **464**(7290), 885–889.
- Nicolas, A. & Christensen, N.I., 1987. Formation of anisotropy in upper mantle peridotites: A review, in *Composition, Structure and Dynamics of the Lithosphere-Asthenosphere System*, pp. 111–123, eds Fuchs, K. & Froideveaux, C., American Geophysical Union.
- Passchier, C.W. & Trouw, R.A.J., 1996. *Microtectonics*, Springer-Verlag.
- Pakiser, L.C. & Robinson, R., 1966. Composition and evolution of the continental crust as suggested by seismic observations, *Tectonophysics*, **3**, 547–557.
- Porter, R., Zandt, G. & McQuarrie, N., 2011. Pervasive lower-crustal seismic anisotropy in Southern California: evidence for underplated schists and active tectonics, *Lithosphere*, **3**, 201–220.

- Reid, M.R., Hart, S.R., Padovani, E.R. & Wandless, G.A., 1989. Contribution of metapelitic sediments to the composition, heat production, and seismic velocity of the lower crust of southern New Mexico, U.S.A., *Earth planet. Sci. Lett.*, **95**(3–4), 367–381.
- Ryzhova, T.V., 1964. Elastic properties of plagioclase, *Bull. Acad. Sci. U.S.S.R.—Izvestia Geophys.*, **7**, 633–635.
- Rudnick, R.L. & Fountain, D.M., 1995. Nature and composition of the continental crust: a lower crustal perspective, *Rev. Geophys.*, **33**, 267–309.
- Savage, M.K., 1999. Seismic anisotropy and mantle deformation: what have we learned from shear wave splitting? *Rev. Geophys.*, **37**, 65–106.
- Schmid, S.M. & Casey, M., 1986. Complete fabric analysis of some commonly observed quartz c-axis patterns, *Geophys. Monogr.*, **36**, 263–286.
- Schulte-Pelkum, V., Monsalve, G., Sheehan, A., Pandey, M.R., Sapkota, S., Billham, R. & Wu, F., 2005. Imaging the Indian subcontinent beneath the Himalaya, *Nature*, **435**, 1222–1225.
- Silver, P.G., 1996. Seismic anisotropy beneath the continents: probing the depths of geology, *Ann. Rev. Earth planet. Sci.*, **24**, 385–432.
- Smithson, S.B., 1978. Modeling continental crust; structural and chemical constraints, *Geophys. Res. Lett.*, **5**(9), 749–752.
- Snoke, A.W., Howard, K.A., McGrew, A.J., Burton, B.R., Barnes, C.G., Peters, M.T. & Wright, J.E., 1997. The grand tour of the Ruby–East Humboldt metamorphic core complex, northeastern Nevada: Part 1—introduction and road log, in *Proterozoic to Recent Stratigraphy, Tectonics, and Volcanology, Utah, Nevada, southern Idaho and central Mexico*, pp. 225–269, Vol. 42, eds Link, P.K. & Kowallis, B.J., Brigham Young University Geology Studies.
- Sullivan, W.A. & Snoke, A.W., 2007. Comparative anatomy of core-complex development in the northeastern Great Basin, U.S.A., *Rocky Mt. Geol.*, **42**(1), 1–29.
- Tatham, D.J., Lloyd, G.E., Butler, R.W.H. & Casey, M., 2008. Amphibole and lower crustal seismic properties, *Earth planet. Sci. Lett.*, **267**, 118–128.
- Theye, T., Parra, T. & Lathe, C., 2003. Room temperature compressibility of clinocllore and chamosite, *Euro. J. Mineral.*, **15**, 465–468.
- Valcke, S.L.A., Casey, M., Lloyd, G.E., Kendall, J.-M. & Fisher, Q.J., 2006. Lattice preferred orientation and seismic anisotropy in sedimentary rocks, *Geophys. J. Int.*, **166**, 652–666.
- Vaughan, M.T. & Guggenheim, S., 1986. The elasticity of muscovite and its relation to crystal structure, *J. geophys. Res.*, **91**, 4657–4664.
- Vaughan, M.T. & Weidner, D.J., 1978. The relationship of elasticity and crystal structure in andalusite and sillimanite, *Phys. Chem. Miner.*, **3**, 133–144.
- Ward, D., Mahan, K. & Schulte-Pelkum, V., 2012. Roles of quartz and mica in seismic anisotropy of mylonites, *Geophys. J. Int.*, **190**, 1123–1134.
- Weiss, T., Siegesmund, S., Rabbel, W., Bohlen, T. & Pohl, M., 1999. Seismic velocities and anisotropy of the lower continental crust: a review, *Pure appl. Geophys.*, **156**, 97–122.
- Wright, J. & Snoke, A., 1993. Tertiary magmatism and mylonitization in the Ruby-East Humboldt metamorphic core complex, northeastern Nevada: U-Pb geochronology and Sr, Nd, and Pd isotope geochemistry, *Geol. Soc. Am. Bull.*, **105**, 935–952.
- Xu, Y., Li, Z. & Roecker, S.W., 2007. Uppermost mantle structure and its relation with seismic activity in the central Tien Shan, *Geophys. Res. Lett.*, **34**, L10304, doi:10.1029/2007GL029708.
- Zhang, S. & Karato, S., 1995. Lattice preferred orientation of olivine aggregates deformed in simple shear, *Nature*, **415**, 777–780.

## SUPPORTING INFORMATION

Additional Supporting Information may be found in the online version of this article:

**Figures S1–S11.** Mineral CPOs for Funeral Mountains, Ruby Mountains and East Humboldt Range samples. Mica, clinopyroxene, calcite, dolomite and sillimanite CPOs are plotted as inverse pole figures with the lineation plotted on the left and the pole to the foliation plotted on the right. Crystallographic directions are marked; directions marked with “\*” indicate the direction normal to the following plane (i.e.  $a^*(100)$  indicates the direction normal to the (100) plane). Plagioclase and K-feldspar CPOs are plotted either as inverse pole figures or equal-area lower hemisphere pole figures. (010) and (001) refer to the pole to the (010) and (001) planes, respectively. Quartz CPOs are always plotted as pole figures. All pole figures are plotted in the same orientation as shown. Shading scale is in MUD and varies between plots.

**Figure S12.** Lower hemisphere contour plots of  $V_P$  (left) and  $V_S$  anisotropy with  $V_{s1}$  polarization directions (right) of Funeral Mountain samples. Top right figure shows the orientation of the plots;  $X$  is the lineation,  $Y$  is perpendicular to the lineation and  $Z$  is normal to the foliation plane (the great circle).

**Figure S13.** Lower hemisphere contour plots of  $V_P$  of East Humboldt Range samples. Top right figure shows the orientation of the plots;  $X$  is the lineation,  $Y$  is perpendicular to the lineation and  $Z$  is normal to the foliation plane (the great circle).

**Figure S14.** Lower hemisphere contour plots of  $V_S$  anisotropy with  $V_{s1}$  polarization directions of East Humboldt Range samples. Top right figure shows the orientation of the plots;  $X$  is the lineation,  $Y$  is perpendicular to the lineation and  $Z$  is normal to the foliation plane (the great circle). (<http://gji.oxfordjournals.org/lookup/suppl/doi:10.1093/gji/ggt287/-/DC1>)

Please note: Oxford University Press are not responsible for the content or functionality of any supporting materials supplied by the authors. Any queries (other than missing material) should be directed to the corresponding author for the article.